UNIVERSITAT POLITÈCNICA DE CATALUNYA BARCELONATECH

Laboratory experiments to evaluate the joint effect between heterogeneity and head fluctuation on mixing, effective porosity and tailing

Eduardo Castro-Alcalá

Ph.D. Thesis

Laboratory Experiments to Evaluate the Joint Effect Between Heterogeneity and Head Fluctuation on Mixing, Effective Porosity and Tailing

Author:
Eduardo Castro-Alcalá

Supervisors:
Dr. Jesús Carrera
Dr. Daniel Fernández-García

Doctorat en Enginyeria Civil

Escola Tècnica Superior d'Enginyers de Camins, Canals i Ports de Barcelona

Barcelona, May 2019

This thesis was funded by the Universitat Politècnica de Catalunya - Escola Tècnica Superior d'Engiyners de Camins, Canals i Ports de Barcelona through the FPU-UPC program.

Abstract

Transport in heterogeneous media under temporally fluctuating velocity fields has been the subject of much research both because ground water fluxes vary naturally in time (evapotranspiration cycles, seasonal variations in rainfall, dry and wet year sequences, or pumping fluctuations) and because it is intuitive that temporal fluctuations of velocity should enhance solute mixing and dispersion.Mixing is increasingly being recognized as the critical process for understanding and modeling reactive transport. Yet, as mixing is highly influenced by the spatial variability of velocity and depends non-linearly on concentrations, its proper characterization remains far from optimal.

Tracer visualization in the laboratory at high spatial and temporal resolution can help advance the study of mixing processes. However, grain borders, fluctuations in lighting and non-uniform brightness contribute to produce noisy images of concentrations that cannot be used to directly estimate mixing at the local scale. We present a new methodology to visualize local values of mixing from noisy images of optical tracers based on a nonparametric regression algorithm. The methodology is used to provide a full visualization of the mixing dynamics that occur in a tracer experiment performed in a reconstructed heterogeneous aquifer consisting of two materials with contrasting hydraulic properties. Results show that the method is capable of providing optimal images of mixing of high quality even at complex material edges between bodies of different sand.

In transport problems, dispersivity control the mixing. Understand the behaviour of this parameter allow characterizing the mixing.Characterize this parameter is complex due to the heterogeneity and the spatial and temporal fluctuations., in that many assumptions (about the definition of dispersion, how to represent it locally, and how to handle medium heterogeneities or velocity fluctuations) are required to make it tractable. Surprisingly the results go in opposite directions.All agree that fluctuations of velocity transverse to the mean flow direction enhance transverse dispersion, some authors conclude that the enhancement is very large, others conclude that it is not so important. Researchers generally agree the effects of velocity fluctuations on longitudinal dispersion is much smaller than on transverse dispersion.But they have found it to decrease. Others increase, others remain unchanged Ironically, despite of all the above research, little experimental work has been performed. For this reason we presents an experiment specifically aimed at evaluating the effect of temporal fluctuations of velocity on transport through a heterogeneous medium and, specifically, on dispersion, mobile porosity and tailing. The results show that Flow fluctuations can enhance transverse mixing and mobile porosity. These phenomena transfer more mass to the plume front, which is now more mobile, and to the low permeability inclusions. As a result, the apparent longitudinal macrodispersion coefficient is substantially increased due to flow fluctuations. Experimental results determined that the effect of flow fluctuations is maximum (enhancement of transverse mixing and macrodispersion) when the kubo number is close to one.

Coastal aquifers are complex zones due to the combined influences of heterogeneity (scale, shape or structure of the aquifer), inland groundwater forces and oceanic oscillations.These produce complex hydrodynamic that effect the location, shape and extent of the dispersion zone. The dynamics (fluctuations, width, and location) of the mixing zone between freshwater and seawater in coastal aquifers is essential for detailed understanding of seawater intrusion and bio-geo-chemical

processes. Yet, results to date are somewhat contradictory.We perform seawater intrusion experiments heterogeneous sand box subject to groundwater flow oscillations. We find that the coupling of heterogeneity and fluctuations leads to complex flow patterns. Freshwater may flow beneath saltwater isolated in low permeability zones when the seawater wedge recedes, but itself become surrounded by seawater when the wedge advances landwards. Fluctuations also disrupt the traditional seawater convection cell, with most of the seawater flow being horizontal, and mixed water displaying some vertical component back to the sea when the seawater wedge recedes seawards.As a result, the mixing zone becomes broad when sea water advances, but narrows down when it recedes. Surprisingly, despite all this complexity the average center of mass of the wedge is very similar to that of the steady-state wedge.

Resumen

El transporte en un medio heterogéneo sometido a fluctuaciones temporales del campo de velocidades está siendo objeto de varias investigaciones, ya que los flujos de agua subterránea varían naturalmente en el tiempo (ciclos de evapotranspiración, variaciones estacionales en la lluvia, secuencias de años secos y húmedos o fluctuaciones locales por los bombeos, etc.) y por qué es intuitivo que las fluctuaciones temporales de la velocidad deberían mejorar la mezcla y dispersión del soluto. La mezcla se reconoce cada vez más como el proceso crítico para comprender y modelar el transporte reactivo. Sin embargo, como la mezcla está altamente influenciada por la variabilidad espacial de la velocidad y depende no linealmente de las concentraciones, su caracterización por ahora está lejos de ser la óptima.

La visualización de un trazador en el laboratorio a alta resolución espacial y temporal puede ayudar a avanzar en el estudio de los procesos de mezcla. Sin embargo, los bordes irregulares de los granos de arena, las fluctuaciones en la iluminación y el brillo no uniforme contribuyen a producir imágenes con ruido en las concentraciones que finalmente no se pueden ser usar para estimar directamente la mezcla a una escala local. Presentamos una nueva metodología para visualizar los valores locales de la mezcla a partir de imágenes con el ruido proveniente de trazadores ópticos basados en un algoritmo de regresión no paramétrico. La metodología se utiliza para proporcionar una visualización de la dinámica de la mezcla que se produce en un experimento con un trazador óptico realizado en un acuífero heterogéneo construido en laboratorio que consta de dos materiales con contraste en sus propiedades hidráulicas. Los resultados muestran que el método es capaz de proporcionar imágenes óptimas de la mezcla de una alta calidad incluso en las zonas donde se localizan los bordes de materiales complejos como entre cuerpos de arena diferente.

En los problemas de transporte, la dispersividad controla la mezcla. Por lo tanto, comprender el comportamiento de este parámetro permitiría caracterizar la mezcla. Caracterizar este parámetro es complejo debido a la heterogeneidad y las fluctuaciones espaciales y temporales, de hecho una cantidad de suposiciones (sobre la definición de la dispersión, cómo representarlo localmente y cómo manejar el medio o las fluctuaciones de la velocidad)son requeridas para hacer manejable el problema. Sorprendentemente, los resultados van en direcciones opuestas. Todos coinciden en que las fluctuaciones de la velocidad transversal a la dirección media del flujo mejoran la dispersión transversal, algunos autores concluyen que la mejora es muy grande, otros concluyen que no es tan importante. Los investigadores generalmente están de acuerdo en que los efectos de las fluctuaciones de la velocidad sobre la dispersión longitudinal son mucho más pequeños que en la dispersión transversal. Pero ellos han encontrado que disminuye. Otros que aumenta, otros que permanece sin cambios. Irónicamente, a pesar de todas las investigaciones anteriores, se ha realizado poco trabajo experimental. Por esta razón, presentamos un experimento específicamente dirigido a evaluar el efecto de las fluctuaciones temporales de la velocidad en el transporte a través de un medio heterogéneo y, específicamente, en la dispersión, la porosidad móvil y las colas. Los resultados muestran que las fluctuaciones en los flujos pueden mejorar la mezcla transversal y la porosidad móvil. Estos fenómenos transfieren más masa al frente de la pluma, que ahora es más móvil en las inclusiones de baja permeabilidad. Como resultado, el coeficiente de macrodispersión longitudinal aparente aumenta sustancialmente debido a las fluctuaciones del flujo. Los resultados experimentales determinaron que el efecto de las fluctuaciones de flujo es máximo (mejora de la mezcla transversal y macrodispersión) cuando el número de kubo está cerca de uno.

Los acuíferos costeros son zonas complejas debido a la influencia que se tiene entre de la hetero-

geneidad (escala, forma o estructura del acuífero), las fuerzas de las aguas subterráneas continentales y las oscilaciones oceánicas. Esta interacción produce una hidrodinámica compleja que afecta la ubicación, la forma y la extensión de la zona de dispersión. La dinámica (fluctuaciones, ancho y ubicación) de la zona de mezcla entre el agua dulce y el agua de mar en los acuíferos costeros es esencial para una comprensión detallada de la intrusión marina y los procesos bio-geoquímicos. Sin embargo, los resultados hasta la fecha son algo contradictorios. Por este motivo, realizamos experimentos de intrusión marina en una caja de arena heterogénea sujeta a oscilaciones en el flujo de agua subterránea. Encontramos que el acoplamiento entre la heterogeneidad y las fluctuaciones conduce a patrones de flujo complejos. El agua dulce puede fluir debajo del agua salada aislada en zonas de baja permeabilidad cuando la cuña de agua de mar retrocede, pero en sí misma queda rodeada de agua de mar cuando la cuña avanza hacia el interior. Las fluctuaciones también interrumpen la celda tradicional de convección de agua de mar, ya que la mayor parte del flujo de agua de mar es horizontal, y el agua mezclada muestra algún componente vertical de regreso al mar cuando la cuña de agua de mar retrocede hacia el mar. Como resultado, la zona de mezcla se ensancha cuando avanza el agua de mar. pero se estrecha cuando retrocede. Sorprendentemente, a pesar de toda esta complejidad, el centro de masa promedio de la cuña es muy similar al de la cuña en estado estacionario

Resum

El transport en mitjans heterogenis sota camps de velocitat temporalment fluctuant ha estat objecte de molta investigació tant perquè els fluxos d'aigües subterrànies varien de forma natural en el temps (cicles d'evapotranspiració, variacions estacionals de precipitacions, seqüències d'anys secs i humits o fluctuacions de bombeig) i perquè és intuïtiu les fluctuacions temporals de la velocitat haurien de millorar la barreja i la dispersió del solut. La mesura es reconeix cada cop més com el procés crític per comprendre i modelar el transport reactiu. Tanmateix, atès que la barreja està molt influenciada per la variabilitat espacial de la velocitat i depèn no linealment de les concentracions, la seva caracterització adequada queda lluny de ser òptima.

La visualització del traçador al laboratori amb una alta resolució espacial i temporal pot ajudar a avançar en l'estudi dels processos de mescla. Tanmateix, els límits del gra, les fluctuacions de la illuminació i la brillantor no uniforme contribueixen a produir imatges sorolloses de concentracions que no es poden utilitzar per estimar directament la barreja a escala local. Presentem una nova metodologia per visualitzar valors locals de barreja a partir d'imatges sorolloses de traçadors òptics basats en un algorisme de regressió no paramètrica. La metodologia s'utilitza per proporcionar una visualització completa de la dinàmica de mescla que es produeix en un experiment de traçador realitzat en un aqüífer heterogeni reconstruït que consta de dos materials amb propietats hidràuliques contrastants. Els resultats mostren que el mètode és capaç de proporcionar imatges òptimes de mescla d'alta qualitat fins i tot en vores de material complex entre cossos de sorra diferent.

En els problemes de transport, la dispersió controla la barreja. Comprendre el comportament d'aquest paràmetre permet caracteritzar la barreja. Caracteritzar aquest paràmetre és complex a causa de l'heterogeneïtat i les fluctuacions espacials i temporals. En aquest cas, molts supòsits (sobre la definició de dispersió, com representar-lo localment i com manejar el mitjà heterogeneïtats o fluctuacions de la velocitat) per fer que sigui tractable. Sorprenentment, els resultats van en direccions oposades. Tots coincideixen que les fluctuacions de la velocitat transversals a la direcció mitjana del flux augmenten la dispersió transversal, alguns autors conclouen que la millora és molt gran, altres conclouen que no és tan important. Els investigadors generalment estan d'acord que els efectes de les fluctuacions de la velocitat en la dispersió longitudinal són molt més petits que en la dispersió transversal. Però el van trobar que es va reduir. Els altres augmenten, altres romanen sense canvis. Irònicament, malgrat tota la investigació anterior, s'ha realitzat poc treball experimental. Per aquest motiu, es presenta un experiment específicament destinat a avaluar l'efecte de les fluctuacions temporals de la velocitat en el transport a través d'un mitjà heterogeni i, específicament, en la dispersió, la porositat mòbil i el tailing. Els resultats mostren que el mètode és capaç de proporcionar imatges òptimes de mescla d'alta qualitat fins i tot en vores de material complex entre cossos de sorra diferent.

Els aqüífers costaners són zones complexes a causa de les influències combinades d'heterogeneïtat (escala, forma o estructura de l'aqüífer), forces d'aigua subterrànies i oscillacions oceàniques. Aquests productes produeixen hidrodinàmica complexa que condiciona la ubicació, la forma i l'extensió de la zona de dispersió. La dinàmica (fluctuacions, amplada i ubicació) de la zona de barreja entre aigua dolça i aigua de mar en aqüífers costaners és essencial per a una comprensió detallada de la intrusió de l'aigua marina i els processos bioquimicoquímics. Tot i així, els resultats fins a la

data són una cosa contradictoris. Realitzem experiments d'intrusió d'aigua marina, heterogènia caixa de sorra subjecte a oscillacions de flux d'aigües subterrànies. Trobem que l'acoblament de l'heterogeneïtat i les fluctuacions condueix a patrons de flux complex. L'aigua dolça pot fluir sota aigua salada aïllada en zones de baixa permeabilitat quan la falca de l'aigua marina es retira, però es troba envoltada d'aigua de mar quan la falca avança cap a terra. Les fluctuacions també interrompen la cèllula tradicional de convecció de l'aigua de mar, ja que la major part del flux d'aigua de mar és horitzontal i l'aigua mixta que mostra un component vertical al mar quan la falca de mar se separa. Com a resultat, la zona de barreja es fa àmplia quan avança l'aigua del mar, però es redueix quan es retira. Sorprenentment, malgrat tota aquesta complexitat, el centre mitjà de massa de la falca és molt similar al de la falca d'estat estable.

Acknowledgments

Firstly I would like to thank my advisors, Jesús Carrera and Daniel Fernández-García. They have been a huge inspiration over the years. They have helped me and encouraged me even in the most difficult moments. I have learned so much by their side.

I shared worries, hopes and a lot of laughter with colleagues who became wonderful friends during my PhD years: Mayka, Kino, Tanguy, Maria, Dani, Anna, Estanis, Marco, Violeta, Chris, Silvia, Jairo, Vlacho, Leo Tanushree. It has been inspirational to have great researchers in the department; people such as Diogo, Xavi, Marco and Tanguy.

The GHS is full of lovely people, always ready to help and listen: Tere, Silvia, Albert, Carles, Manuel, and the guys in the lab.

Of course I wouldn't have survived all these years without the unconditional support of my lovely family: Gabi, Nidia, Carolina. Family who always listen to my stories, provide useful advice and most importantly, make me laugh when I need it.

Thanks to my friends who cheered me up throughout my thesis: Lucio, Darvis, Carlos, Manuel.

"*Le compuse estos versos a Paquito*" ... Meta cumplida Papá

Contents

Abstract i

Resumen iii

Resum v

Acknowledgments vii

1 Introduction 1
1.1 Background . . . 1

2 Visualization of mixing processes in a heterogeneous sand box aquifer 5
2.1 Introduction . . . 5
2.2 Experimental procedure . . . 6
2.2.1 Sand-box . . . 6
2.2.2 Tracer experiment . . . 8
2.2.3 Image acquisition . . . 8
2.3 Image processing . . . 8
2.3.1 Methodology . . . 9
2.3.2 Selection of a color channel . . . 9
2.3.3 Relationship between light intensity and concentrations . . . 9
2.3.4 Reconstruction of mixing from noisy images . . . 11
2.4 Results . . . 13
2.5 Conclusions . . . 19

3 Effect of Temporal Flow Fluctuations on Transport Behavior in a Synthetic Heterogeneous Aquifer. 21
3.1 Introduction . . . 21
3.2 Experimental Methods . . . 22
3.2.1 Physical Model . . . 22
3.2.2 Tracer Experiment . . . 23
3.2.3 Image acquisition and image processing . . . 25
3.3 Interpretacion Methods . . . 26
3.3.1 Effective porosity . . . 26
3.3.2 Kube Number . . . 26
3.3.3 Conceptual transport models . . . 27
3.4 Results . . . 30
3.4.1 Temporal Evolution of resident concentrations . . . 30
3.4.2 Behavior of breakthrough curves . . . 32
3.4.3 Effect on macrodispersion, local dispersion and mixing . . . 33
3.4.4 Effect on macrodispersion, local dispersion and mixing . . . 37
3.4.5 Conclusion . . . 37

4 Heterogeneous Sand Box Experiments on the Impact Flux Fluctuations on the dynamics of the Mixing zone in Coastal Aquifers. 39
4.1 Introduction . . . 39
4.2 Experimental procedure . . . 40
4.2.1 Experimental Tank . . . 41
4.2.2 Tracer Experiment . . . 41
4.2.3 Image acquisition and Image processing . . . 42
4.3 Results and discussion . . . 44
4.4 Conclusions . . . 47

5 Conclusions 49

Bibliography 51

List of Figures

2.1 Schematic experimental setup of the sand box: (a) Front view; (b) Top view. Measurements are in centimeters. 7
2.2 Sensitivity of light intensity during Rhodamine injection for one representative pixel associated with coarse sand. 10
2.3 Calibration curves on concentration against normalized pixel intensity for representative pixels located in both the high and low permeability zones. 10
2.4 Equivalent weights $\mathbf{W}^{(0)}$ used to calculate concentrations and concentration gradients in equations (7), (8) and (9) associated with three different pixels located within the mixing zone. 14
2.5 Image map of concentrations (left hand side) and mixing (right hand side) obtained at time 16 minutes and 54 seconds for different methods: (1) Non-filtered data; (2) 11×11 Moving Window Average; (3) 51×51 Moving Window Average; (4) Proposed Methodology. 15
2.6 Temporal evolution of concentrations (left hand side) and mixing (right hand side) during the initial 42 minutes of Rhodamine injection and the following 42 minutes of flushing with freshwater. 16
2.7 comparison of the global mixing measure R_{mix} with MWA using a windows of 11×11 pixels and 51×51 pixels 18
2.8 comparison of the global mixing measure R_{mix} with MWA using a windows of 11×11 pixels and 51×51 pixels 19

3.1 Schematic experimental setup and distribution of the fine send inclusions conforming the aquifer 23
3.2 Illustration of the flow fluctuation function used during experiment 1 (steady-state flow conditions) and 4 (with a pulse duration of 6 minutes) 25
3.3 Sequence of the sand box images taken at selected times during the course of the experiments 1 and 4, and processed into concentration maps. 31
3.4 Comparison of tracer breakthrough curves obtained with and without flow fluctuations 33
3.5 Best fit between experimental data (depth resident concentrations) and the effective ADE model 34
3.6 Best fit between experimental tracer breakthrough curves measured at the tank outlet (red) with the effective ADE model (black line) and the MRMT model (blue). . . . 36

4.1 Schematic experimental setup of the sand box for seawater experiment. 42
4.2 Behavior of seawater wedge for four different times. (A) S.S conditions; (B) Seawater wedge average for S.S fluctuation; (C) Maximum intrusion; (D) Minimum intrusion 43
4.3 Evolution of seawater wedge in different times. Graphics present a different points in the evolution cycle. For each point we present the seawater wedge position . . . 45
4.4 Profile concentration Evolution of seawater wedge in different times. This profile was stored in a Matrix (N,M). N is pixel (z) number, and M is time steps 48

List of Tables

3.1 Properties of the two type of sands used 22
3.2 Experimental flow and tracer conditions 24
3.3 Transport parameters calibrated against experimental data using the effective ADE model; Macrodispersivity is obtained from depth-average resident concentrations and local dispersivity from the early arrival of breakthrough curves. 35
3.4 Transport parameters calibrated against experimental data (tracer breakthrough curves measured at the tank outlet) using the MRMT model with a truncated power-law probability density function of mass transfer rates 37

Chapter 1

Introduction

1.1 Background

Coastal aquifers are undergoing rapid changes due to increasing population, high water demand with expanding agricultural and domestic uses, and seawater intrusion due to unmanaged water pumping. The combined impact of these activities is the deterioration of groundwater quality, public health concerns, and unsustainable water demands. These aquifers are still subject to dynamic due to pumping, and because groundwater fluxes vary naturally in time. Head gradients fluctuate in time at range of scales: daily, as a result of evapotranspiration cycles or earth tides; yearly, as result of seasonal variations in recharge, or hyperannually, as a result of dry and wet year sequences By the other hand the aquifer are structure highly complex.to make a model hydrographically complex. The heterogeneity is present a different scales, preferential paths, lateral an vertical variations of facies, paleochannels, etc. This heterogeneity added to head variations produce complex velocity fields that inside on mixing Proper characterization of the mixing processes occurring in the subsurface is crucial for a comprehensive description of a large variety of biogeochemical problems, including cave formation, calcite precipitation and dolomization (Runnels, 1969; Hanshaw and Back, 1979; Raeisi and Mylroie, 1979; Ayora et al., 1998; Willingham et al., 2008; Zhang et al., 2010a), chemical speciation and microbial reactions (Nnambi et al., 2003; Knutson et al., 2005; Aucour et al., 2003; Cirpka and Frind, 1999; Raje and Kapoor, 2000; Jose and Cirpka, 2004) among others.

What emerges from these works is that the rate of reactions, their location and the conditions under which they occur all depend not only on chemistry but also on the rate of mixing (Rezaeia et al., 2005). (De Simoni et al., 2005) showed that the vector of reaction rates per unit volume of fluid, r, associated with a binary chemical system (c1c2) can be expressed as

$$\mathbf{r}(\ \mathbf{x}, t) = \mathbf{F}_{chem}\mathbf{F}_{mix}, \qquad \mathbf{F}_{mix} = \nabla^T \mathbf{u}\mathbf{D}\nabla\mathbf{u} \tag{1.1}$$

Where $\mathbf{u}$ is the concentration of the conservative component, and $\mathbf{D}$ is the diffusion (hydrodynamic dispersion) tensor. This expression states that reaction rates are actually determined by the product of two terms: one term $\mathbf{F}_{chem}$ that only depends on the speciation of the reactive species and another term $\mathbf{F}_{mix}$ that measures mixing, caused by the joint effect of the local concentration gradients and diffusion (dispersion).

$\mathbf{F}_{mix}$ describes mixing at the local scale, which is directly related to the reaction rates occurring at a given location and time. Global mixing (i.e., the integral of over the entire domain) is proportional to the dissipation rate time derivative of the global concentration variance, regardless of the type of flow field (Le Borgne et al., 2010). Is clear that to define $\mathbf{F}_{mix}$ is necessary obtain the gradients of concentrations, the problem is that these are highly influenced by the natural variability of the aquifer properties. Although the relationship between physical heterogeneity and mixing remains undefined, it is well known that the Advection-Dispersion equation provides a poor representation of mixing at all scales. This has been shown in homogeneous column experiments (Gramling et al., 2002) and in numerical simulations and stochastic analyses of solute transport

performed in heterogeneous media (Fernàndez-Garcia et al., 2008; Luo et al., 2008). The problem in these experiments is that a good representation of the mixing requires detailed knowledge of concentrations gradients. But the geometric properties of the porous media, light fluctuation, variations in brightness due to nonuniform light sources, among a variety of others problems, produce noisy estimates of concentrations. These noise is after increase in gradient concentration produce false values of mixing. For this reason the first objective of this thesis is to present a methodology aimed at fully visualizing mixing from light intensity images of optical tracers. This methodology is then applied to visualize the mixing dynamics occurring in a tracer experiment performed in a heterogeneous sand-box aquifer.

Temporal fluctuations of velocity fields can be intuitively that should enhance solute mixing and dispersion (Dagan, 1989; Dentz and Carrera, 2003; Cirpka and Attinger, 2003), facilitating the spreading of solutes injected in a water body and mixing with resident water.

Characterizing dispersion has concentrated efforts in groundwater hydrology, driven by spatial variability of permeability mostly assuming steady flow (see, e.g., Dagan (1989); Gelhar (1993)), or turbulence, driven by random temporal fluctuations mostly assuming homogeneous fluids (e.g., book by Pope,). However, much less effort has been devoted to acknowledging both spatial and temporal fluctuations. This probably reflects that problem is complex, in that many assumptions (about the definition of dispersion, how to represent it locally, and how to handle medium heterogeneities or velocity fluctuations) are required to make it tractable (De Dreuzy et al., 2012a).

Therefore, it is not surprising that their findings are disparate. All agree that fluctuations of velocity transverse to the mean flow direction enhance transverse dispersion: numerical analyses conclude that the enhancement is very large (Kinzelbach and Ackerer, 1986; Goode and Konikow, 1990; De Dreuzy et al., 2012a) stochastic researchers conclude that it is not so important (Cirpka and Attinger, 2003; Dagan et al., 1996; Zhang and Neuman, 1996). Researchers generally agree the effects of velocity fluctuations on longitudinal dispersion is much smaller than on transverse dispersion. But they have found it to decrease (Zhang and Neuman, 1996; De Dreuzy et al., 2012a), decrease or increase (Goode and Konikow, 1990; Rehfeldt and Gelhar, 1992), increase (Dentz and Carrera, 2005) or remain unchanged (Cirpka and Attinger, 2003).

Ironically, despite of all the above research, little experimental work has been performed to evaluate how temporal fluctuations affect mixing, mobile porosity and tailing. Thereby, the second objective of this thesis is to present an experiment specifically aimed at evaluating the effect of temporal fluctuations of velocity on transport through a heterogeneous medium and, specifically, on dispersion, mobile porosity and tailing.

Finally, Coastal aquifers are complex zones due to the combined influences of heterogeneity (scale, shape or structure of the aquifer), inland groundwater forces and oceanic oscillations. These produce complex hydrodynamic that effect the location, shape and extent of the dispersion zone (or mixing zone) that in turn influences contaminant transport from the aquifer to the coastal sea and different chemical processes in the mixing zone.

While it is generally agreed that the mixing zone is critical for detailed understanding of SWI and bio-geo-chemical processes, the controls of its width and dynamics remain a subject of debate. (Abarca et al., 2007; Paster and Dagan, 2008) argue that the width of the mixing zone is mainly controlled by transverse pore-scale dispersion, which yields a relatively narrow mixing zone. This would support the sharp interface approximation and is consistent with laboratory experiments performed in homogeneous media (Volker, 2002; Goswami and Clement, 2007; Abarca and Prabhakar Clement, 2009), but inconsistent with field observations, which often display broad (more than 10 m) mixing zones (Xue et al., 1993; Price et al., 2003; Langevin, 2003; Kim et al., 2007), to name a few).

Similar to what happened with dispersion in SWI exists disparity between field and theory has been attributed to heterogeneity and groundwater flow fluctuations driven by either sea-level fluctuations or inland fluctuations in recharge and pumping Yet, stochastic (Dell'Oca et al., 2018), numerical simulations (Abarca et al., 2007) and laboratory experiments (Rahman et al., 2005b) conclude that heterogeneity does not cause a significant enhancement of transverse dispersion. Instead, SWI research has concentrated on the impact of fluctuations. (Li et al., 1999) showed that groundwater circulation and oscillating flows can greatly increase the rate of chemical transfer to the ocean. (Andersen et al., 2005)A argued that water level fluctuations enhance the width of mixing zone and affect many chemical reactions. (Moore, 1973), showed that beach rock cementation depends on the mixing of ocean and aquifer water. (Ataie-Ashtiani and Ketabchi, 2010) use a numerical model to show that tidal fluctuations forces the seawater to intrude further inland and create a thicker interface than would occur without tidal effects. These results contradict theoretical findings, which conclude that fluctuations do not cause dispersion in homogeneous media but simply cause plumes to be dragged back and forth without spreading (see discussion by de De Dreuzy et al. (2012b)), which is consistent with both numerical simulations and laboratory experiments (Kuan et al., 2012).

(María et al., 2015) analyzed the joint effect of heterogeneity and groundwater flow fluctuations and concluded that, contrary to the findings of (Ataie-Ashtiani and Ketabchi, 2010), the net effect of fluctuations in heterogeneous media is a displacement seawards of the SWI wedge, but that little effect was observed on the width of the mixing zone, which they attributed to the connectivity of 3D media, which led to relatively large values of hydraulic conductivity. Finally the third objective of this thesis is to describe the results of laboratory experiments on a heterogeneous sand box to analyze the effect of groundwater flow fluctuations on the mixing zone, its dynamics, width and location.

This thesis is structured as three papers that have been published or are in the publications process.

- Chapter 2 (base on Castro et al., 2012) contains a nonparametric regression methodology to visualize local values of mixing from noisy images of optical tracer that minimizes smoothing in the direction of concentration gradients.
- Chapter 3 focus on evaluating from laboratory experiments the effect of temporal fluctuations of velocity on transport through a heterogeneous medium and, specifically, on dispersion, mobile porosity and tailing.
- Chapter 4 presents a laboratory experiments on a a heterogeneous sand box to analyze the effect of groundwater flow fluctuations on the mixing zone, its dynamics, width and location
- Chapter 5 presents the general conclusions of the thesis deduced from the previous chapters.

Because of this structure, a good deal of information is repeated, especially site description. I leave it to the discretion of the reader to skip repeated information. On the other hand, the advantage of this structure is that chapters can be read independently.

CHAPTER 2

Visualization of mixing processes in a heterogeneous sand box aquifer *

2.1 Introduction

Proper characterization of the mixing processes occurring in the subsurface is crucial for a comprehensive description of a large variety of biogeochemical problems, including cave formation, calcite precipitation and dolomization (Runnels, 1969; Hanshaw and Back, 1979; Raeisi and Mylroie, 1979; Ayora et al., 1998; Willingham et al., 2008; Zhang et al., 2010a), chemical speciation and microbial reactions (Nnambi et al., 2003; Knutson et al., 2005; Aucour et al., 2003; Cirpka and Frind, 1999; Raje and Kapoor, 2000; Jose and Cirpka, 2004) among others. What emerges from these works is that the rate of reactions, their location and the conditions under which they occur all depend not only on chemistry but also on the rate of mixing(Rezaeia et al., 2005). Several measures of mixing can be found in the literature (Weeks and Sposito, 1998; Cirpka and Frind, 1999; Raje and Kapoor, 2000; Gramling et al., 2002) . When transport can be fully defined in terms of conservative components (i.e., when all reactions are locally instantaneous and in equilibrium) and mixing of all solute species is locally controlled by diffusion (or dispersion), (De Simoni et al., 2005) showed that the vector of reaction rates per unit volume of fluid, $\mathbf{r}$, can be expressed as

$$\mathbf{r}(\ \mathbf{x}, t) = \mathbf{F}_{chem}\mathbf{F}_{mix}, \qquad \mathbf{F}_{mix} = \nabla^T \mathbf{u}\mathbf{D}\nabla\mathbf{u} \tag{2.1}$$

where $\mathbf{u}$ is the vector of conservative components, $\mathbf{D}$ is the diffusion (hydrodynamic dispersion) tensor, and $\mathbf{F}_{chem}$ is the Hessian matrix involving second derivatives of concentration of solute species with respect to concentrations of conservative components $\mathbf{u}$. This expression states that reaction rates are actually determined by the product of two terms: one term that only depends on the speciation of the reactive species $\mathbf{F}_{chem}$ and another term $\mathbf{F}_{mix}$ that measures mixing, caused by the joint effect of the local concentration gradients and diffusion (dispersion). This measure of mixing appears repeatedly in the literature and will be the subject of this paper. (Kapoor and Gelhar, 1994) demonstrated that the variance of concentrations follows an Advection-Dispersion Equation (ADE) with an $\mathbf{F}_{mix}$ related sink term that is responsible for smearing the concentrations in aquifers. Similarly, Sanchez-Vila et al.(Sanchez-Vila et al., 2009) found that the probability density function of the concentrations of reactive and conservative species satisfies a non-local ADE with a source term related to $\mathbf{F}_{mix}$. The probability of occurrence of "mixed" concentrations was found to increase with $\mathbf{F}_{mix}$. This measure of mixing is also included in the dilution index ratio proposed by Kitanidis (Kitanidis, 1994), which is closely related to entropy. It is a measure that quantifies the degree of dilution in a system reflecting the apparent volume occupied by the solute, aiding one to distinguish effectively between macrodisperive spreading (effective plume size) and mixing. (Kitanidis, 1994) defines the degree of dilution as being quantified by:

*This Chapter is based on the paper Castro-Alcalá et al. (2012)

$$E(t) = \exp\left(-\int_v p\ln(p)d\mathbf{x}\right); \quad p(\mathbf{x},t) = \frac{u(\mathbf{x},t)}{\int_v u(\mathbf{x},t)d\mathbf{x}} \tag{2.2}$$

Instead, $\mathbf{F}_{mix}$ describes mixing at the local scale, which is directly related to the reaction rates occurring at a given location and time. Global mixing (i.e., the integral of over the entire domain) is proportional to the dissipation rate time derivative of the global concentration variance, regardless of the type of flow field (Le Borgne et al., 2010).

In real field settings, the gradients of concentrations involved in the definition of $\mathbf{F}_{mix}$ are highly influenced by the natural variability of aquifer properties. In real field settings, the gradients of concentrations involved in the definition of are highly influenced by the natural variability of aquifer properties. In general, the erratic velocity fields typically obtained in natural aquifers produce highly distorted solute plumes that enhance mixing, e.g. (Luo et al., 2008). Although the relationship between physical heterogeneity and mixing remains undefined, it is well known that the Advection-Dispersion equation provides a poor representation of mixing at all scales. This has been shown in homogeneous column experiments (Gramling et al., 2002) and in numerical simulations and stochastic analyses of solute transport performed in heterogeneous media (Fernàndez-Garcia et al., 2008; Luo et al., 2008).

The lack of an appropriate quantification of mixing compromises the reliability of reactive transport simulations. Thus, more fundamental studies of mixing through laboratory experiments are needed. A promising laboratory method for understanding mixing is tracer visualization at high spatial and temporal resolutions. The method consists of visualizing the migration of an optical tracer injected into a porous medium. A full picture of the solute distribution is obtained by analyzing the relationship between pixel intensity and tracer concentration in time and space. The problem with these techniques is that the roughness and geometric properties of the porous media, light fluctuations and variations in brightness due to non-uniform light sources among a variety of other problems produce noisy estimates of concentrations. Several attempts have been made in the past to reduce this noise. (McNeil et al., 2006) propose to segment the image optically, (Rahman et al., 2005a) used both a geometric correction and color calibration, Schincariol et al. (1993) suggested a general median smoothing to 3×3 pixels to reduce the noise associated with glass bead sizes, (Konz et al., 2008) filtered the image using a window averaging technique consisting of 10×10 pixels. All these approaches were designed to improve the estimates of concentrations but none of them are well suited to directly estimate mixing. A complete representation of mixing requires detailed knowledge of concentration gradients, which cannot be directly estimated from noisy images.

The objective of this paper is to present a methodology aimed at fully visualizing mixing from light intensity images of optical tracers. This methodology is then applied to visualize the mixing dynamics occurring in a tracer experiment performed in a heterogeneous sand-box aquifer.

2.2 Experimental procedure

2.2.1 Sand-box

The tracer experiment was conducted in an unconfined heterogeneous aquifer reconstructed in the laboratory using two types of sand with contrasting hydraulic properties. The sand distribution in the tank consists of a rectangular inclusion of fine sand (low permeability) embedded in an otherwise highly permeable coarse sand. The objective of this particular distribution is to visualize and quantify the mixing dynamics occurring at the interface between two distinct materials with

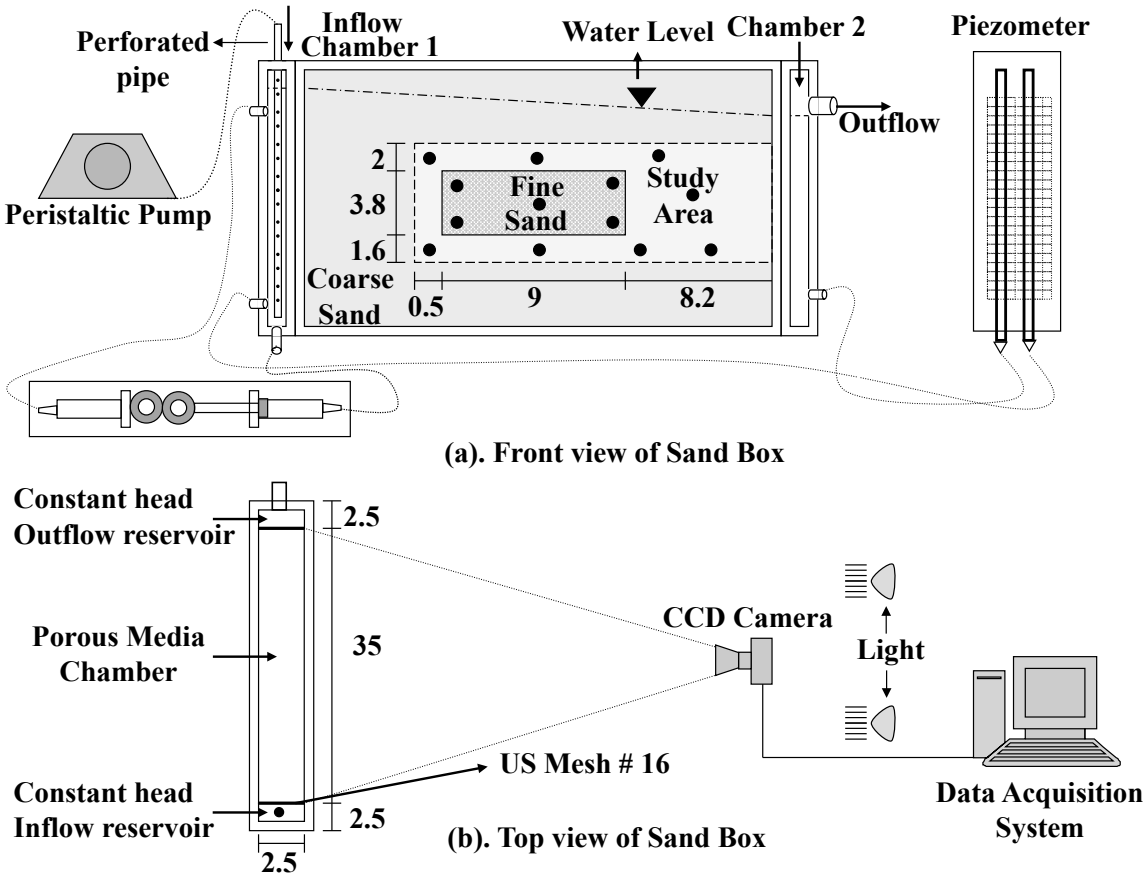

Figure 2.1: Schematic experimental setup of the sand box: (a) Front view; (b) Top view. Measurements are in centimeters.

contrasting hydraulic properties.

The sand box containing the aquifer is a quasi two-dimensional vertical tank of length 36.5 cm, height 27 cm and width 2.5 cm, fully made of transparent $plexiglass^{TM}$. The sand-box was divided into three distinct areas. Figure 2.1 shows a sketch diagram of the experimental setup. The central chamber is 32.5 cm long and contains the reconstructed aquifer. Two stainless steel meshes $US\#16$ separate the influent and effluent chambers from the central flow chamber. The influent and effluent chambers serve to prescribe the head boundary conditions needed to run the tracer experiment.

A sieve analysis determined that the sand is poorly graded with a coefficient of uniformity of 1.2 and 1.25 for the coarse and fine sands, respectively. Grain diameters range from 1.0 to 1.2 mm for the coarse sand, and from 0.4 to 0.6 mm for the fine sand. A constant head permeameter cell was used to determine the hydraulic conductivity of the sands, obtaining 1060 m/day and 67.5 m/day for the coarse and fine sand, respectively. The tank was packed under fully saturated conditions layer by layer to avoid trapping of air and minimize segregation. The porosity was estimated gravimetrically as 0.4.

2.2.2 Tracer experiment

Rhodamine B (Panreac) was injected into the sand-box aquifer. This compound can effectively be considered as a conservative tracer because it neither adsorbs nor degrades in clean quartz sand The tracer experiment proceeded as follows. First, water was pumped into the aquifer at a constant rate of 49 mL/min through a perforated vertical pipe into chamber 1 This produced a constant head of 24.15 cm at the inflow reservoir and 23 cm at the outflow reservoir. Once steady state conditions were achieved, Rhodamine B was continuously injected into the aquifer at a concentration of 200 mg/L for 42 minutes at the same flow rate. After this, the tank was flushed with freshwater. The start and stop of tracer injection were carefully executed to minimize head perturbations. For this, two connected sets of syringes were employed to rapidly extract and replace the fluid in chamber 1 with the desired solution (with a transient of roughly 5 seconds).

2.2.3 Image acquisition

The $plexiglass^{TM}$ structure of the sand box permits visualization of the migration of the optical tracer without a disturbance of the mixing dynamics inside the aquifer. Many authors have utilized optical tracers to visualize and quantify solute concentrations in synthetic aquifers (Schincariol et al., 1993; Swartz and Schwartz, 1998; McNeil et al., 2006; Rahman et al., 2005a; Konz et al., 2008). Light transmission or reflected light are the two techniques used to obtain map concentrations. Here, we choose reflected light for image analysis so that we may analyze a generic non transparent sand material with different mineralogy and texture. We tested four different types of light sources (incandescent, halogen, fluorescent and LEDs). Best results in terms of sensitivity, temperature and fluctuations were obtained with LEDs. Some LEDs properties are uniform spectral power distribution from 380 to 780 nm, the light colour remains constant,good heat dissipation, a higher luminous flux, and better luminous efficacy. Two LEDs light sources were placed at a distance of 20 cm from the tank.
A CCD camera (AVT Guppy F-080B/C) was used to continuously record the red (R), green (G), and blue (B) color images of the tracer experiment. A computer programme (AVT SmartView v1.7.2) controls the image acquisition and transfer of information to a computer. We set all parameters manually (relative aperture F5.6, shutter speed 1/30). These parameters are the same for both calibration and image processing of the experiment. Images were acquired every six seconds both during the initial 42 minutes of Rhodamine injection and the following 42 minutes of flushing with freshwater. The camera and the tank are fixed to a fixed metal structure that is placed inside a black room to fully control the light intensity emitted to and reflected from the tank. The black room is located inside a temperature controlled lab and ventilated with fans to ensure a constant temperature. The spatial resolution of the camera is 1024×728 pixels so that each pixel represents an area of $0.32 \times 0.32\ mm^2$ and has a color resolution of 8 bits. Thus, the RGB color channels range linearly between 0 to 255 in terms of values of intensity.

2.3 Image processing

The concentration interpretation of optical tracers is based on the relationship between light intensity and tracer concentration (Schincariol et al., 1993; McNeil et al., 2006; Konz et al., 2008; Gramling et al., 2002; Rahman et al., 2005a). The application of a such relationship in porous media can be cumbersome because light intensity is affected by factors other than absorption and reflection of a light ray passing through a fluid with tracer concentrations. In particular, the light

rays reflected in the tank and entering the camera to form an image are also influenced by the roughness and geometric properties of the sand grains, fluctuations in the source light, and brightness variations due to nonuniform lightning that introduce noise.

2.3.1 Methodology

Here, we use a locally adapted kernel regression technique specifically designed to optimally smooth mixing.The procedure we use to estimate mixing follows five principle steps: [1] Capture the image in raw data and convert it to 8 bit BMP images; [2] select the channels most sensitive to the tracer; [3] determine the relationship between light intensity and concentrations for each image pixel; [4] use the light intensity relationships to map the concentrations; and [5] reconstruct mixing from noisy images of concentrations. Since our objective is to examine the occurrence of mixing at the interface between materials, we restricted our image processing analysis to the study area depicted in Figure 2.1.

2.3.2 Selection of a color channel

Preliminary tracer tests revealed that substantial differences exist between the signals in each of the three color channels. Figure 2.2 shows the channel signal observed for the red, green, and blue channel as a function of time during the tracer experiment. The signal is sorted by the soil type of the corresponding chosen pixel. The green channel was seen to be the most sensitive, likely because the maximum absorption wavelength of *Rhodamine B* (565 nm) is close to the wavelength of the excitation light (545 nm). Figure 2.2 also shows that the green channel provides a less noisy response than the blue and red spectrum. Based on this, we chose to work with the green channel signal.

2.3.3 Relationship between light intensity and concentrations

In order to account for the spatial variations of light intensity and the influence of an underlying non-transparent porous medium, we analyzed the relationship between light intensity and concentrations pixel by pixel. This was found crucial for analyzing this type of experiments. These relationships were calibrated before running the experiment by injecting eleven known solutions of Rhodamine B into the sand-box aquifer (0, 10.13, 19.79, 30.47, 38.7, 8.83, 87.86, 120, 147.8, 179.19, 199.87 mg/L). These solutions were independently injected in the tank from low to high concentrations. For each solution, a continuous injection was performed until a steady-state image of reflected light intensity was obtained. The resulting images $I_1(\mathbf{x}), ..., I_{11}(\mathbf{x})$ constituted the reference light intensity for the given solution of Rhodamine. The final relationship was obtained by a piece-wise of the data points as

$$C(I;\mathbf{x}) = C(I_i;\mathbf{x}) + \frac{C(I_{i+1};\mathbf{x}) - C(I_i;\mathbf{x})}{I^*_{i+1}(\mathbf{x}) - I^*_i(\mathbf{x})} \times (I^*(\mathbf{x}) - I^*_i(\mathbf{x})), \qquad I^*(\mathbf{x}) \in [I^*_i(\mathbf{x}), I^*_{i+1}(\mathbf{x})] \quad (2.3)$$

where $C(I;\mathbf{x})$ is the concentration of Rhodamine at location $\mathbf{x}$ for a light intensity I, and I^* is a normalized light intensity, defined as $I^*_i = I_i/I^0_i$. The light intensity I^0 is the light intensity of a blank image obtained under steady-state flow conditions before the injection (taken as the average over 60 minutes). This normalization aims to remove any small temporal variations in the energy supply that can substantially affect light intensity (Konz et al., 2008). Figure 2.3 shows the calibration curves obtained for several pixels in the study area. The large width of the ensemble illustrates the importance of calibrating this relationship pixel by pixel for this type of experiments.

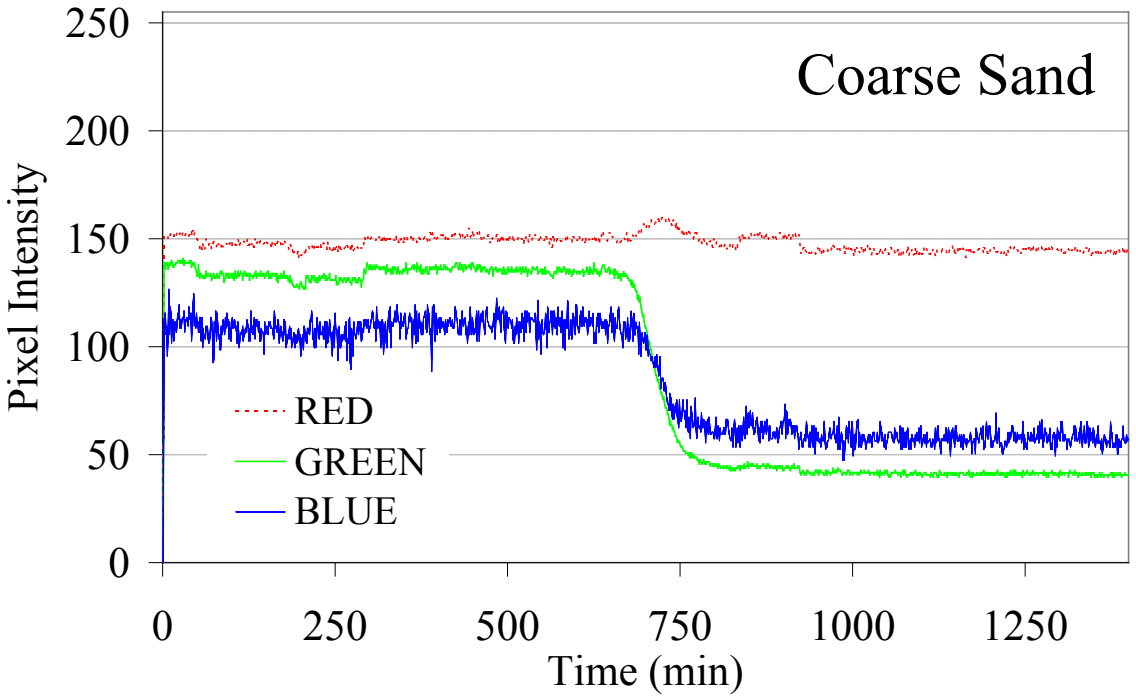

Figure 2.2: Sensitivity of light intensity during Rhodamine injection for one representative pixel associated with coarse sand.

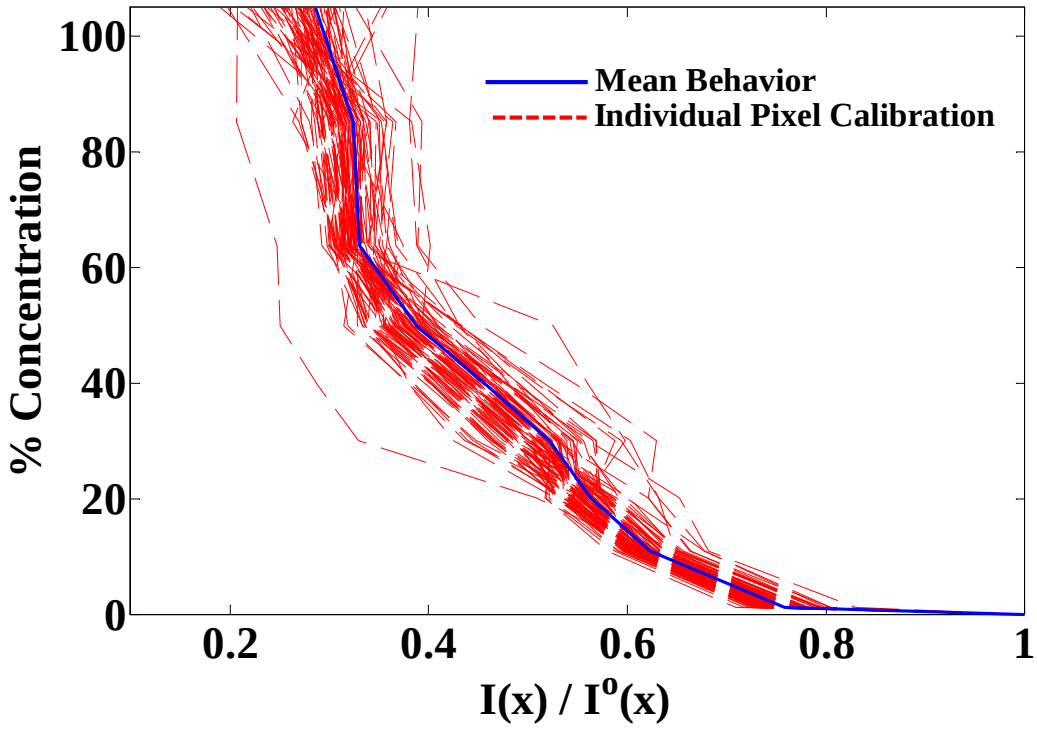

Figure 2.3: Calibration curves on concentration against normalized pixel intensity for representative pixels located in both the high and low permeability zones.

2.3.4 Reconstruction of mixing from noisy images

Concentration fields, $u(\mathbf{x})$, can be estimated from noisy images $C(I;\mathbf{x})$ using a suite of parametric and non-parametric methods (Hardle, 1991). All of them involve either local regressions, filtering of noise, or both. A shared drawback is that they may produce some degree of oversmoothing or bias of the concentration field and the mixing rate (Equation 2.3). To minimize this effect, we propose here a methodology that attempts to obtain the best of two existing methods:

(1) The "Steering Kernel Regression" method (SKR) of Takeda et al. (2007), which is based on weighting concentration measurements in the direction of concentration isolines, ensures that no smoothing is produced in the concentration gradient direction. Although this method provides high quality images, it does not provide a clear way to optimally define smoothing parameters.

(2) The weighted kernel density estimation method (wKDE) is capable of automatically selecting the optimal level of smoothing, but fails to optimally orient the kernel function. As a result gradients may be smoothed out in areas where concentrations gradients are not aligned with the mean flow direction.

The proposed approach consists of two stages. during first stage, the wKDE method is applied to small areas of the image, where concentration isolines are aligned with the x axis, and where the wKDE method works well (Fernàndez-Garcia and Sanchez-Vila, 2011). The size of these areas is (100×100 pixels) and their centroid are shown in as black circles. The mixing rate,$\mathbf{F}_{mix}^{wKDE}$, is evaluated at these points. At the second stage, themore sophisticated data-adaptiveSKR method is used, selecting its smoothing parameters so as to match $\mathbf{F}_{mix}^{SKR}$ with $\mathbf{F}_{mix}^{wKDE}$ as closely as possible. Details of both methods are outlined below. Optimality of the WKDE method is presented as supporting material.

2.3.4.1 Weighted Kernel Density estimation

Let $p = \phi u/M$ be the normalized concentration of an image recorded at time t, where M is the mass of tracer at time t, known from the experimental mass balance of the optical tracer, and ϕ is the porosity. Then, the problem of reconstructing mixing is reduced to the estimation of p and its gradient $\nabla p = [p_x, p_y]^T$ given a sample of pixel values. The focus here will be on,

$$\mathbf{F}_{mix}^{wKDE} = \| \nabla u \|^2 = M^2 \| \nabla p \| / \phi^2 \tag{2.4}$$

which is related to local reactions by (3). Estimation of p and ∇p can be optimized easily for 1D problems. Fernández-Garcia and Sanchez-Vila (Fernàndez-Garcia and Sanchez-Vila, 2011) generalized 1D optimal methods by viewing concentrations as a cumulative probability distribution function and using the definition of the conditional density function $p(x,y) = p(y|x)p(x) = p(x|y)p(y)$, where $p(x|y)$ and $p(y|x)$ are the conditional density functions, and p(x) and p(y) are the marginal density functions, which leads to,

$$u(x,y,t) = M/\varphi\sqrt{p(y|x)p(x)p(x|y)p(y)}, \tag{2.5}$$

$$\mathbf{F}_{mix}^{wKDE}(x,y,t) = M^2(p(y|x)p_x(x)p_x(x|y)p(y) + p(x|y)p_y(y)p_y(y|x)p(x))/\phi^2, \tag{2.6}$$

The wKDE estimator of the marginal probabilities, for instance $p(x)$ and $px(x)$, are obtained from the normalized pixel data $p_i = p(\mathbf{x}_i)$ as

$$p(x) = kk \sum_{i=1}^{n} \frac{P_i}{h_0} K\left(\frac{x_i - x}{h_0}\right), \quad p_x(x) = kk \sum_{i=1}^{n} \frac{P_i}{h_1^2} K'\left(\frac{x_i - x}{h_1}\right), \tag{2.7}$$

where K is a weight function, chosen as a zero mean unit variance Gaussian, K' its derivative, and h_0 and h_1 are respectively the level of smoothing for p and p_x. Using the mean integrated squared error criterion to evaluate the expected error of these estimators, the optimal supports are (Engel et al., 1994),

$$h_0 = \left(\frac{R(K)}{(kk_2(K))^2 R(p''n)}\right)^{1/5}, \quad h_1 = \left(\frac{3R(K'3!^2)}{4(kk_3(K'))^2 R(p'''n)}\right)^{1/7}, \tag{2.8}$$

where $R(g)$ and $kk_n(g)$ are the L2-norm and the nth-absolute moment of g. These optimal estimates involve the unknown function pwhich needs to be further estimated. To this end we used the plug-in algorithm described in Engel et al. (1994) for this purpose. The use of Equation(2.5)-Equation(2.7) to estimate mixing has been already thoroughly tested against analytical solutions and shown to outperform traditional methods (Fernàndez-Garcia and Sanchez-Vila, 2011) for concentration fields described in terms of particles. The fields here are not made up of particles, however, this limitation can be overcome by expanding the sample data pi in terms of constant mass particles (Wang and Wang, 2008). That is, prior to the reconstruction of $\mathbf{F}_{mix}^{wKDE}$, a new image was generated by uniformly distributing ni pixel values of equal weight, $p = 1/N$, in each pixel cell according to $n_i = p(x,t)N$, where N being the total number of data points used (N=50000) in the specific area.

2.3.4.2 Steering Kernel Regression

In nonparametric regression, the measured normalized concentrations are expressed as a local Taylor expansion around the estimation location **x**plus a noise term. Assuming a quadratic form of the regression model

$$p_i = \beta_0 + \beta_1 x'_i + \beta_2 y'_i + \beta_3 x'^2_i + \beta_4 x'_i y'_i + \beta_5 y'^2_i + e_i, ...), \quad i = 1, ..., n, \tag{2.9}$$

where e_i is an independent and identically distributed zero mean noise values, $\mathbf{x}'_i = \mathbf{x}_i - \mathbf{x}$ is the distance from the estimation location, β_0 is the estimated pixel value at $\mathbf{x}$, $[\beta 1, \beta 2]T$ its corresponding gradient and so on. In matrix form, this is simplified to

$$\mathbf{p} = \mathbf{Xb} + \mathbf{e}, \quad \mathbf{X} = \begin{bmatrix} 1 & \mathbf{x}'_1 & \mathbf{y}'_1 & (\mathbf{x}'_1)^2 & (\mathbf{x}'_1)(\mathbf{x}'_1) & (\mathbf{y}'_1)^2 \\ ... & ... & ... & ... & ... & ... \\ 1 & \mathbf{x}'_n & \mathbf{y}'_n & (\mathbf{x}'_n)^2 & (\mathbf{x}'_n)(\mathbf{x}'_n) & (\mathbf{y}'_n)^2 \end{bmatrix} \tag{2.10}$$

where $\mathbf{b} = [\beta_0, \beta_1, \beta_2, \beta_3, \beta_4, \beta_5]^T$, $\mathbf{p} = [p_1, ..., p_n,]^T$, and $\mathbf{e} = [e_1, ..., e_n,]^T$. The regression parameter vector $\mathbf{b}$ is typically obtained by minimizing the weighted sum of squared residuals, i.e., $SSE = \mathbf{e}^T\mathbf{We}$, where $\mathbf{W}$ is a given weight matrix. The solution of this optimization problem is

$$\mathbf{b} = (\mathbf{X}^T\mathbf{WX})^{-1}\mathbf{X}T\mathbf{Wp} \tag{2.11}$$

Since $\mathbf{b}$ and the regression function are expressed as a local weighted average of the data, the coefficients multiplying $\mathbf{p}$ in (10) can be denoted as equivalent weights. Nonparametric regression evaluates $\mathbf{b}$ at the estimation location $\mathbf{x}$ from only nearby data. A natural way to do this is to give nearby samples higher weight than samples further away so that

$$\mathbf{W} = diag\left\{K(\mathbf{x'}_1), ..., K(\mathbf{x'}_n)\right\} \tag{2.12}$$

where K is a weight function typically assumed as a Gaussian kernel,

$$K(\mathbf{x'}_1) = \frac{1}{2\pi\sqrt{\det\left(\mathbf{H}_i\right)}} \exp\left[\frac{\mathbf{x'}_i^T \mathbf{H}_i^{-1} \mathbf{x'}_i}{2}\right], \tag{2.13}$$

and $\mathbf{H}$ is the smoothing matrix. Whenever $\mathbf{H}$ is constant and does not depend on data values, the quality of the reconstruction in areas with complex geometries is low. To solve this problem, Takeda et al. (2007) proposed to locally rotate and scale $\mathbf{H}$ to ensure that weight is concentrated along concentration isolines,

$$\mathbf{H}_1^{-1} = \frac{1}{\mu^2}\left[\nabla u \nabla u^T\right]_{x=x_i} \tag{2.14}$$

where the overbar stands for averaging over the pixels adjacent to $\mathbf{x}_i$, μ is a global smoothing parameter.This filter is nonlinear because $\mathbf{H}_i$ depends now on the solution through ∇u . Therefore, its application is iterative. Figure 2.4 shows the maps of equivalent weights obtained for three different pixels located in the mixing zone at time 12 minutes 6 seconds. Remarkably, these weights are able to adapt themselves to the presence of fine sand, even at the corner boundary, which ensures that little weight is given to concentration values inside the fine sand, thus preventing the smothing of gradients. The mixing property can be finally estimated as

$$\mathbf{F}_{mix}^{SKR} = \nabla u^2 = M^2\left(\beta_1^2(x,y) + \beta_1^2(x,y)\right)/\phi^2 \tag{2.15}$$

The global smoothing parameter μ 4is chosen so as to obtain $\mathbf{F}_{mix}^{SKR}$ images similar to obtained at the selected areas during the first stage. We found that a value of μ equal to 3.6 pixels with 4 iterations provided optimal results.

2.4 Results

We applied the kernel regression image processing techniques described in section 2.3 to the experimental setup in section 2.2, to map concentrations as well as mixing. While the acquired images capture the full experimental setup, we focus our analysis and discussion only on the study area highlighted in Figure 2.1, which incorporates the boundaries between materials of contrasting permeability. Images were acquired every six seconds during both the initial 42 minutes of Rhodamine injection and the following 42 minutes of flushing with freshwater. Initially the tank is filled with freshwater that has zero Rhodamine content. Figure 2.5 shows the results obtained at 16 minutes and 54 seconds after injection. Here, the results of our proposed methodology are compared with those obtained directly from the calibrated images (non-filtered data) and those obtained using a moving window average technique (MWA), which is the standard technique used in previous visualization experiments (Schincariol et al., 1993; Konz et al., 2008). It consists simply of averaging the pixel values over a moving window. The gradients needed to estimate mixing in these cases were approximated by finite differences. We consider two possible windows consisting of 11×11 pixels and 51×51 pixels. The first window resembles previous studies to estimate concentrations (Konz et al., 2008). The other provides a sufficiently smooth image with negligible noise. Although at first sight the 11×11 MWA provides reasonable images of concentrations, their local fluctuations are still too high to estimate mixing properly. On the contrary, the 51×51 MWA shows zero noise

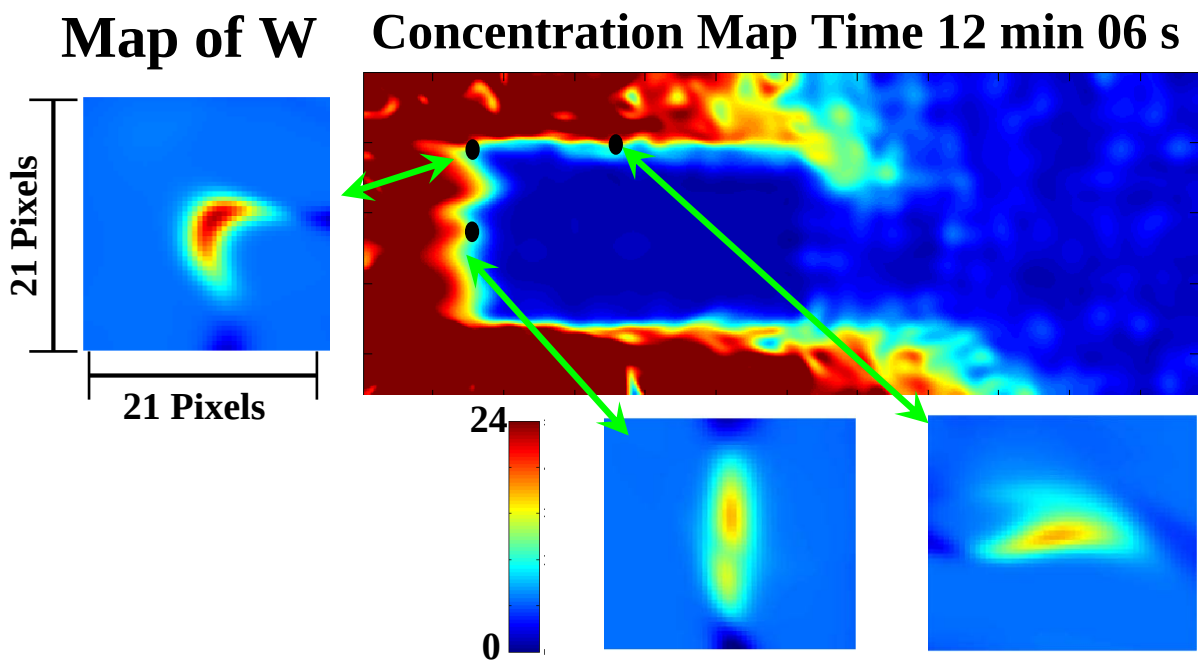

Figure 2.4: Equivalent weights $\mathbf{W}^{(0)}$ used to calculate concentrations and concentration gradients in equations (7), (8) and (9) associated with three different pixels located within the mixing zone.

but at the expense of substantially oversmoothing mixing. Our proposed methodology is able to eliminate most of the fluctuations while still providing an adequate description of mixing.

The ability to visualize concentrations and mixing so clearly using our iterative optimal kernel algorithm highlights the strength of the algorithm for these types of experiment.

The typical evolution of the concentration field by the injection and flushing is shown in 2.6 over the entire course of the experiment. The tracer takes 7.2 minutes to arrive to the low permeability sand inclusion and another 26.63 minutes to actually occupy the fine sand. The tank is completely full after 40 minutes. At early times the effect of macrodispersive spreading is evident as contaminant travels through the high permeability zones quickly, taking much longer to enter the low permeability zone, highlighting visually the fundamental difference between mixing and spreading. This causes strong gradients (particularly in the transverse direction) at the interface between the two materials. While the tracer takes relatively little time to cross the tank through the high permeability areas, it takes much longer for the tank to completely fill with Rhodamine due to the slower processes associated with the low permeability zone. This is strongly reminiscent of the mobile/immobile concepts often used in multi-rate mass transfer type models which have been relatively successfully extended to mixing driven reactions (Willmann et al., 2010). It is also important to highlight that the region directly downstream of the low permeability inclusion looks somewhat like a wake in that it takes a long time to fill and that strong transverse gradients persist here also. In this region, the solute traveling across the high permeability area in the tank is able to mix with an almost stagnant freshwater that is still resides behind the inclusion.

The flushing process that begins after 42 minutes is qualitatively similar to the initial injection period, although a close look at the images in Figure 2.5 indicates some small differences. For

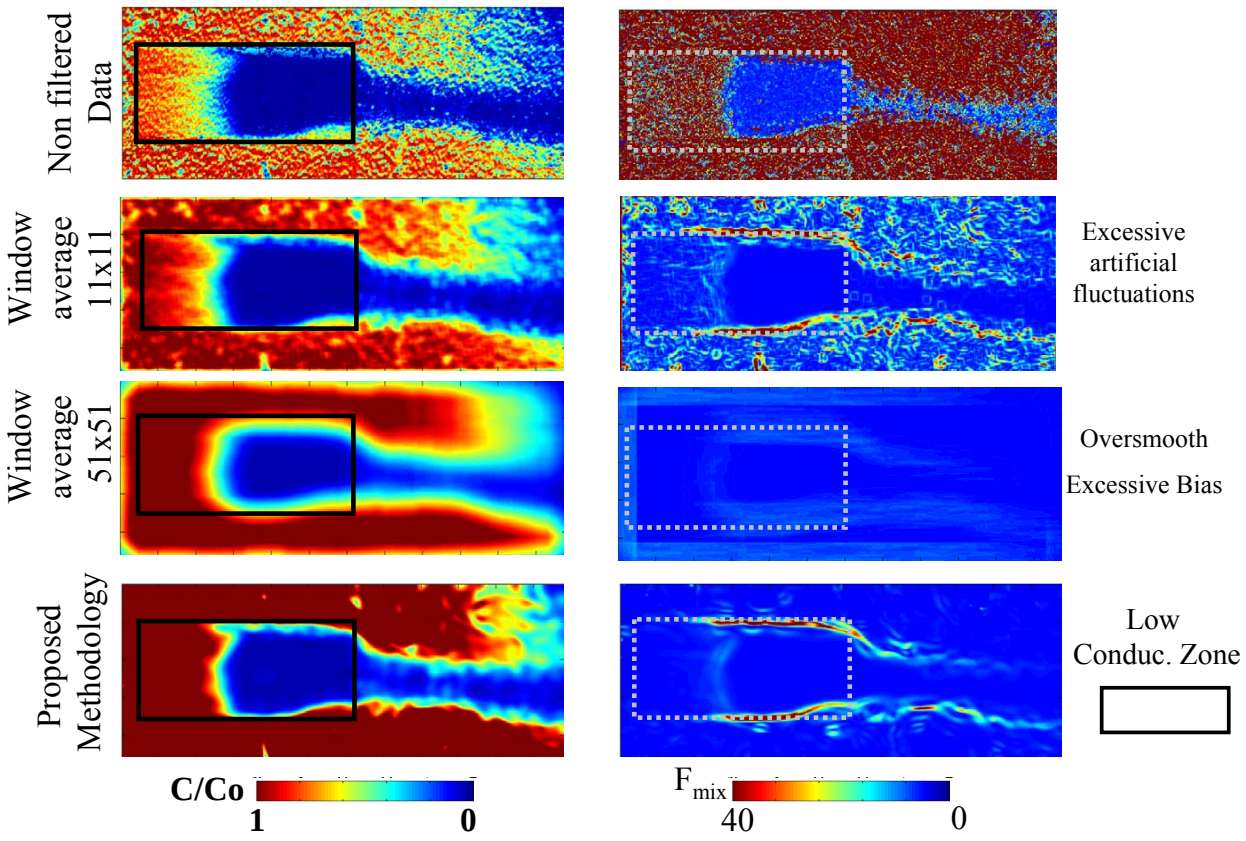

Figure 2.5: Image map of concentrations (left hand side) and mixing (right hand side) obtained at time 16 minutes and 54 seconds for different methods: (1) Non-filtered data; (2) 11×11 Moving Window Average; (3) 51×51 Moving Window Average; (4) Proposed Methodology.

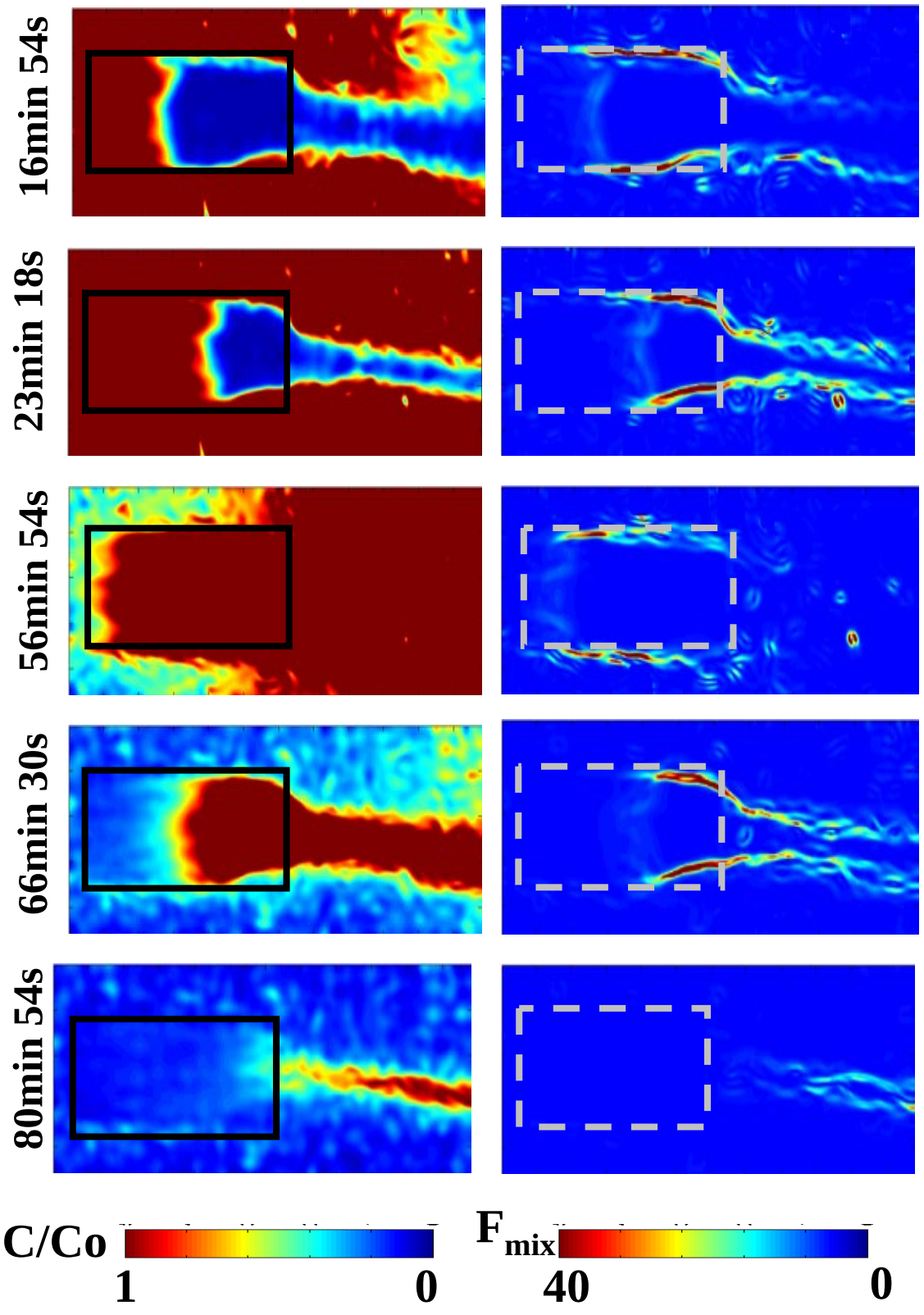

Figure 2.6: Temporal evolution of concentrations (left hand side) and mixing (right hand side) during the initial 42 minutes of Rhodamine injection and the following 42 minutes of flushing with freshwater.

instance, remaining fluctuations, manifested by hot round spots in the mixing image, are distributed in a different manner during the injection and flushing period. This can likely be attributed to the shape of the calibration curve, where high concentrations are more sensitive to light intensity. Thus, more noise is always observed in areas filled with Rhodamine. We note that the optimality of μ is based on a global criterion and therefore some local artificial fluctuations may still be produced.

These strong transverse gradients have significant implications with regard to reactive transport. As highlighted in the introduction and mathematically illustrated in equation 2.1 the rate of reaction is directly proportional to the gradient squared. Therefore, from Figure 2.6 we can infer that the regions of greatest reaction are not just at the mixing front advancing in the direction of flow as would be the case for a homogeneous medium, but specifically along interfaces between zones of differing permeability. This result is consistent with geological observations such as the formation of Mississippi Valley Type deposits (Corbella et al., 2004) or permeability enhancement at the base of weathering fronts in plutonic rocks (Lachassagne et al., 2011) From the mixing images it is immediately obvious that these transverse gradients are dominant and that peak reaction rates are most likely to occur at interfaces with high permeability contrast. This in turn agrees with previous comments that transverse mixing is a fundamental driver of hydrogeochemical reactions, e.g.(Jose and Cirpka, 2004; Zhang et al., 2010b).

Along with the local rate of mixing we can also estimate a global measure of mixing, which may be of more interest at the large scale. To this end we use a global measure of mixing that is the integral of the concentration gradient squared over the study area,

$$R_{mix}(t) = \int \mathbf{F}_{mix}(\mathbf{x}, t) d\mathbf{x} \tag{2.16}$$

We compare our result of R_{mix} with both, no filter dat and MWA using a windows of 11×11 pixels and 51×51 pixels (Figure 2.7). The noise present in the non processes image produce a high value of R_{mix} and that the different between the injection and the flushing is not clear. By the other hand use MWA with a windows of 51×51 produce a lower value due to the zero noise and substantially oversmoothing mixing (Figure 2.5). The real value of R_{mix} should be over this value. while using a windows of 11×11 produce local fluctuations on concentrarion gradients that are still too high to estimate mixing properly (Figure 2.5). Due to this the value real value of R_{mix} should be under this value. Our technique produce a value of R_{mix} located in the middle of these two MWA. Due to our technique reduce the noise in concentration and F_{mix}, we think that our result is very near to the real value of F_{mix}

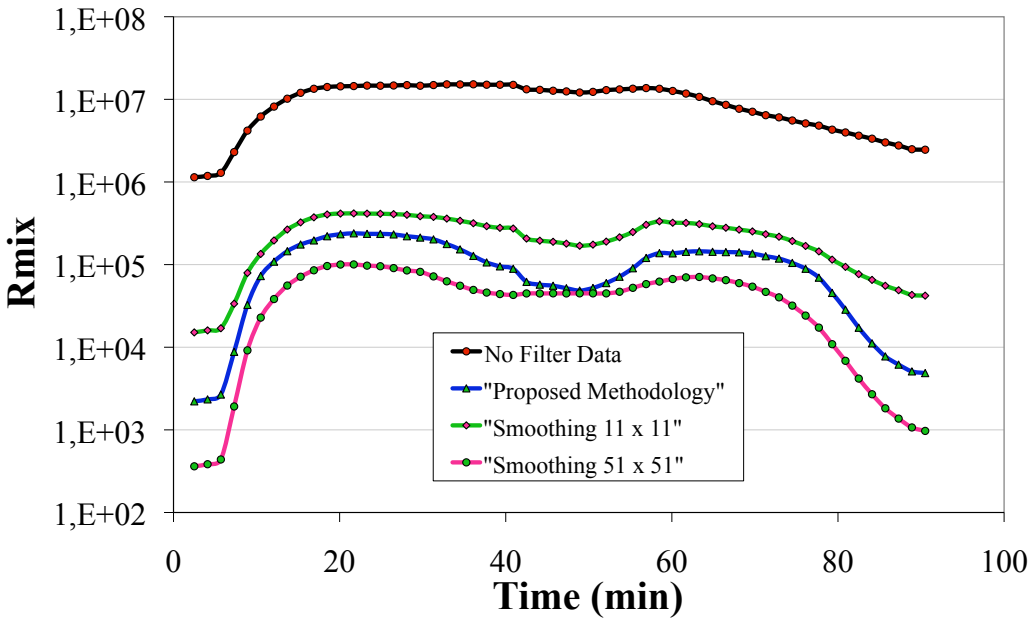

Figure 2.7: comparison of the global mixing measure R_{mix} with MWA using a windows of 11×11 pixels and 51×51 pixels

Such global measures have been used in previous numerical and theoretical studies and shown to play an important role in the global rate of reaction (Fernàndez-Garcia et al., 2008; Bolster et al., 2010; Le Borgne et al., 2010). As mentioned in the introduction, the dilution index can also be used to quantify the degree of mixing.
To understand what controls the rate of dilution of a solute in time,(Kitanidis, 1994) defined it as the rate of change of logarithmic of the dilution index, i.e.

$$R_E(t) = \frac{d\ln(E)}{dt} \tag{2.17}$$

Figure 2.8 shows the dilution rate and the global measure of mixing rate over time for our tracer test. For early times, the distortion of the concentration field associated with the advection field causes the dilution rate to decrease with time with respect to the initial homogeneous well-mixed behavior.
The minimum dilution rate (time=7.3 min) occurs when the propagating front comes in contact with the low transmissivity zone. After that, from time=7.3 min onwards, strong vertical concentration gradients begin to form and there is a rapid increase in both the dilution ratio $R_E(t)$ and the global mixing rate $R_{mix}(t)$. Both measures of mixing start increasing over the same time, but with substantially differing late-time behavior after the hump. That is, global mixing Rmix shows a more persistent effect with time since strong transverse gradients can continuously occur over the entire interface between materials. While the rate of volume occupied by solute undergoes a sudden hump when the tracer rapidly passes through the high permeability zone, the concentration

gradients persist until the tracer is able to finally occupy the low permeability zone, later on, due to slow advection. Remarkably, the peak of $R_{mix}(t)$ occurs at time=23 min, right when the solute has partially filled the low permeability area through slow advection and is able to further mix with the almost stagnant freshwater residing behind the inclusion. Interestingly, the behavior of R_E and R_{mix} is different. While the dilution rate effectively measures the rate of change of the plume volume, which is very high during injection until the solute tracer reaches the low permeability region, this low permeability region generates strong gradients that enhance mixing over larger periods of time. The opposite occurs during flushing. The tracer lagging behind slows down the dilution rate until it is fully washed out. As a result R_E lags behind R_{mix} during flushing. This observation highlights that the two quantities are different but complementary.

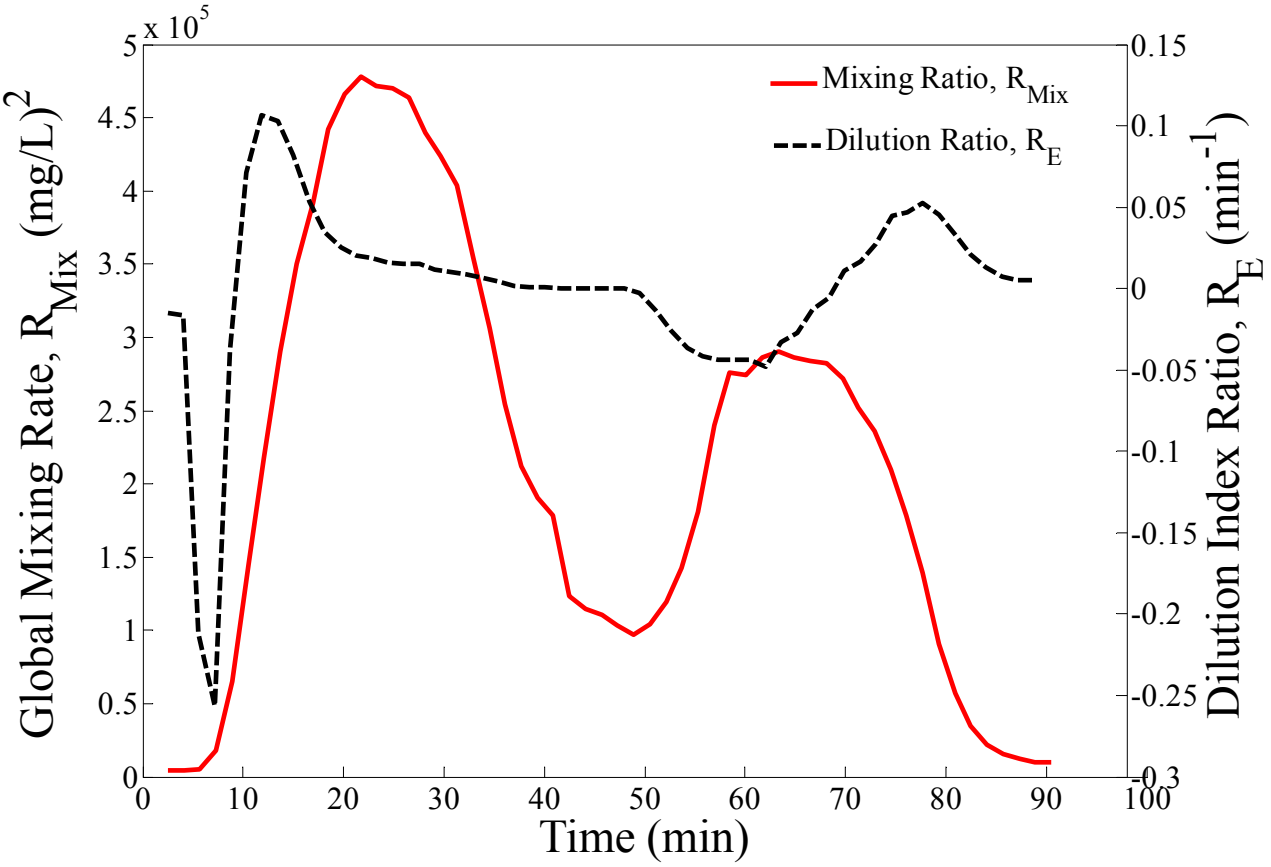

Figure 2.8: comparison of the global mixing measure R_{mix} with MWA using a windows of 11×11 pixels and 51×51 pixels

2.5 Conclusions

The understanding of mixing processes is one of the current major challenges in subsurface hydrology. Tracer visualization is a convenient technique that is typically used to analyze processes in the laboratory. However, these techniques typically provide noisy images that only reliably quantify concentrations. They cannot be used to directly quantify mixing as this depends strongly on concentration gradients, which are very sensitive to noise. This article presents a novel methodology to overcome these problems. They can be used to investigate reactive transport processes under a

variety of hydraulic and chemical conditions. The method is applied to visualize, the local mixing processes that occur during the injection and flushing of tracer in a heterogeneous porous medium. Several important conclusions should be highlighted from this work. First, we have shown that while traditional image processing techniques do not provide proper mixing estimates, our optimal methodology can actually depict local mixing processes. Moreover, the experiment demonstrates that transverse gradients can be dominant at interfaces with high permeability contrasts within aquifers as well as in areas of relatively low velocity. As a result, regions of greatest reactions should not be expected only at the mixing front advancing in the direction of flow, as would be the case for a homogenous medium, but also along interfaces between zones of differing permeability. The experiment was also used to analyze the temporal evolution of two well known mixing indices, i.e., the dilution index ratio and the global mixing rate. The peak of dilution was seen to occur relatively quickly after injection when the plume was most distorted by the spatially varying velocity field. In contrast, the peak of the global mixing rate occurred later when slow advection and mixing with stagnant water were the most active transport mechanisms.

Chapter 3

Effect of Temporal Flow Fluctuations on Transport Behavior in a Synthetic Heterogeneous Aquifer.

3.1 Introduction

Transport in heterogeneous media under temporally fluctuating conditions has been the subject of much research both because ground water fluxes vary naturally in time (evapotranspiration cycles, seasonal variations in rainfall, dry and wet year sequences, or pumping fluctuations) and because it is intuitive that temporal fluctuations of velocity should enhance solute mixing and dispersion. Characterizing dispersion has concentrated efforts in stochastic groundwater hydrology, driven by spatial variability of permeability, mostly assuming steady-state flow e.g., Dagan (1989); Gelhar (1993), or in turbulent flow, driven by random temporal fluctuations, mostly assuming homogeneous fluids (e.g., Pope (2000)).

However, much less effort has been devoted to acknowledging the interplay of both spatial and temporal fluctuations. This probably reflects that the problem is complex in that many assumptions (about the definition of dispersion, how to represent it locally, and how to handle medium heterogeneities or velocity fluctuations) are required to make it tractable (De Dreuzy et al., 2012a). Therefore, it is not surprising that their findings are disparate. All agree that fluctuations of velocity transverse to the mean flow direction enhance transverse dispersion: numerical analyses conclude that the enhancement is very large e.g., (Cirpka and Attinger, 2003; Dagan et al., 1996; Zhang and Neuman, 1996) but stochastic theories conclude that it is not so important (Cirpka and Attinger, 2003; Dagan et al., 1996; Zhang and Neuman, 1996). Researchers generally agree that the effects of velocity fluctuations on longitudinal dispersion is much smaller than on transverse dispersion, but they have found it to decrease (Zhang and Neuman, 1996; De Dreuzy et al., 2012a), decrease or increase (Goode and Konikow, 1990; Rehfeldt and Gelhar, 1992), increase (Dentz and Carrera, 2005) or remain unchanged (Cirpka and Attinger, 2003).

Ironically, despite of all the above research, little experimental work has been performed to give further insights into the problem. Carefully monitored plumes at Borden (Canada) found that lateral spreading was much larger than predicted by stochastic theories and they attributed this to the fluctuations in the direction of the hydraulic gradient (Sykes et al., 1982; Sudicky, 1986; Rehfeldt and Gelhar, 1992). The paucity of experimental work probably reflects the above mentioned difficulties. Even worse, the emphasis on dispersion may be misguided because it is becoming generally agreed that the Advection-Dispersion-Equation (ADE) is a very partial description of transport. Specifically, it fails to acknowledge mixing, which is essential for reactive transport. Thus the search for transport description is shifting towards non-local formulations such as the Multi-Rate Mass Transfer (MRMT) model that seeks to represent the observed early solute arrival through a mobile porosity and late tails through mass-exchange terms with immobile regions (Haggerty and Gorelick, 1995; Carrera et al., 1998; Haggerty et al., 1998; Dentz et al., 2000; Willmann et al., 2008;

Donado et al., 2009; Fernàndez-Garcia et al., 2009; De Dreuzy et al., 2012a; Fernaàndez-Garcia and Sanchez-Vila, 2015).

The question of how temporal fluctuations affect mobile porosity has not been even posed. The objective of our work is to present an experiment specifically aimed at evaluating the effect of temporal fluctuations of velocity on transport through a heterogeneous medium and, specifically, on dispersion, mobile porosity and tailing.

3.2 Experimental Methods

3.2.1 Physical Model

Laboratory tracer experiments were conducted in a reconstructed heterogeneous unconfined aquifer embedded in a two-dimensional vertical tank made of plexiglass with dimensions of $34.7 \times 22.5 \times 3.5cm^3$ ($L \times H \times W$). A sketch of the experiment is shown in Figure 3.1. The clear plexiglass pane facilitates the visual observation of the tracer transport through the heterogeneous porous media during the experiments. The tank has three different chambers. The influent and effluent chambers serve to prescribe the head boundary conditions needed to run the tracer experiment. The central chamber contains the reconstructed aquifer. Two stainless steel meshes $US\#16$ separate the influent and effluent chambers from the central flow chamber. Figure 3.1 shows a sketch diagram of the experimental setup. The heterogeneous aquifer was reconstructed in the laboratory with two types of sand with contrasting hydraulic properties.

Table 3.1: Properties of the two type of sands used

Parameter	Units	Value
Hydraulic conductivity of coarse sand	m/day	1060
Hydraulic conductivity of fine sand	m/day	67.5
Gravimetric porosity	-	0.4
Volume fractions of coarse sand	-	0.66
Volume fractions of fine sand	-	0.34
Variance of the natural log of K	-	1.7
Longitudinal average size of a fine sand lens	cm	4.7
Vertical average size of a fine sand lens	cm	2.0

A sieve analysis determined that the sand is poorly graded with a uniform coefficient of 1.2 and 1.25 for the coarse and fine sand, respectively. The grain diameter of these sands ranges from 1.0 mm to 1.2 mm for the coarse sand, and from 0.6 mm to 0.4 mm for the fine sand. The hydraulic conductivities of the sands obtained by a constant head permeameter cell is 1060 m/day and 67.5 m/day for the coarse and fine sand, respectively. The heterogeneity consists of 29 different rectangular inclusions of fine sand (low permeability) embedded in a matrix of highly permeable coarse sand. The volume fraction of the fine sand is 34%, which renders a heterogeneous system with a variance of the natural log of hydraulic conductivity of 1.7. The average size of an individual lens is 4.7 cm and 2.0 cm in the longitudinal and vertical direction, respectively. The objective of this particular distribution is to create a tortuous solute path similar to a real system. The tank was packed under fully saturated conditions using a metallic template grid and conducted sequentially layer by layer to avoid air trapping and minimize segregation. The porosity

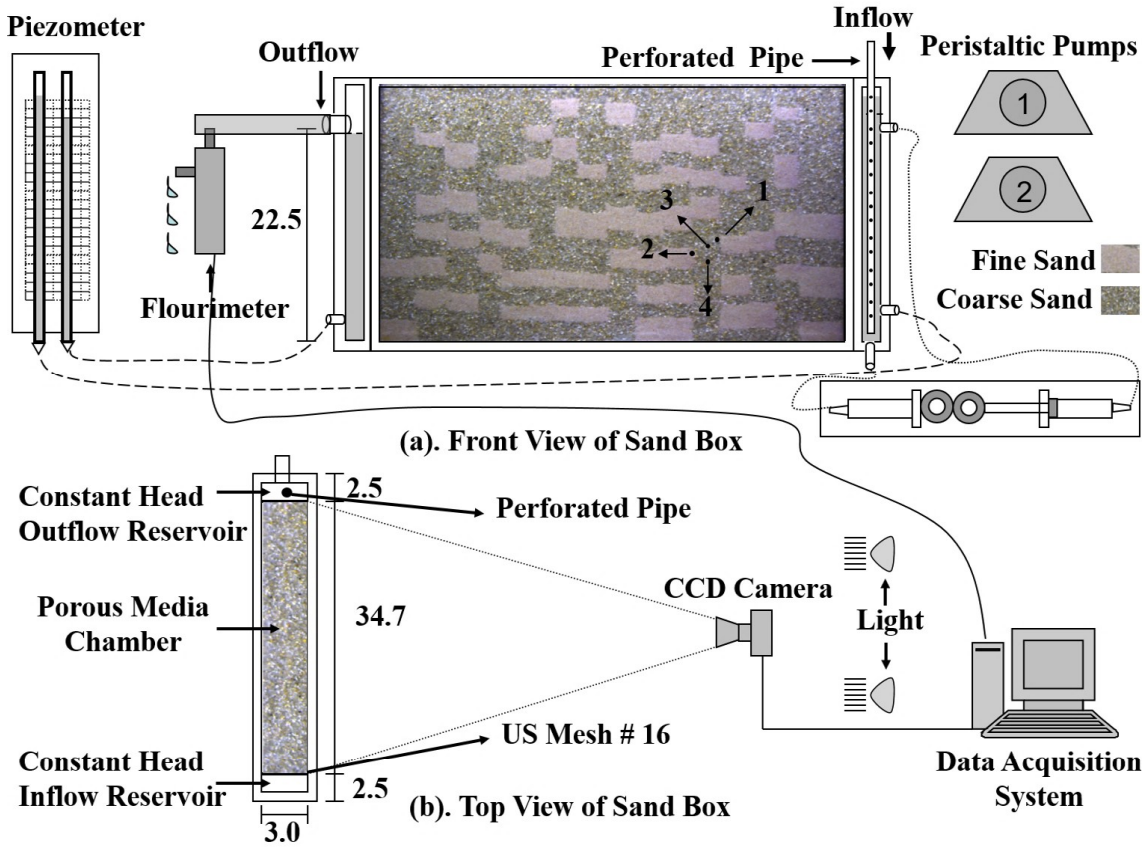

Figure 3.1: Schematic experimental setup and distribution of the fine send inclusions conforming the aquifer

was estimated gravimetrically as 0.4. Properties of the two types of sands are presented in Table 3.1.

3.2.2 Tracer Experiment

Four different tracer experiments were conducted to assess the joint effect of flow fluctuations and heterogeneity on solute transport. Tracer experiments consisted in the injection of the same volume of tracer solute (Rhodamine B, *Panreac*) into the aquifer subject to different flow fluctuations. Experiment 1 injected water with a constant flow rate (steady-state flow conditions) while experiments 2, 3 and 4 were conducted with a flow rate that fluctuates according to a symmetric square wave function characterized by a pulse duration τ. The pulse function can be formally expressed by its corresponding Fourier series expansion, written as

$$Q_{inj}(t) = Q_{inj}^{min} + (Q_{inj}^{max} - Q_{inj}^{min}) f(t;\tau) \tag{3.1}$$

where

$$f(t;\tau) = \frac{1}{2} + \sum_{n=1}^{\infty} \frac{2}{n\pi} \sin\left(\frac{n\pi}{2}\right) \cos\left(\frac{n\pi t}{\tau} - \frac{n\pi}{2}\right) \tag{3.2}$$

Figure 3.2 shows an illustration of the fluctuation function of the total injection flow rate. Table

3.2 summarizes the experimental parameters used. We used Rhodamine B (Panreac) because this solute neither adsorbs nor degrades in clean quartz sand; it can effectively be considered as a conservative tracer. For each experiment, we measured tracer breakthrough curves (BTCs) at the tank outlet using a fluorimeter. We also recorded high-resolution images of the tracer concentrations with time using a charge-coupled device (CCD) camera. For each experiment, before the injection of tracer, we continuously pumped dionized water into the tank for 60 minutes to assure steady-state flow conditions at the start of the experiment. From this time, a slug of Rhodamine B was injected into the aquifer with a concentration of 200 mg/L. After that, the tank was flushed with deionized water. The total injection flow rate was maintained constant during experiment 1. However, in experiments 2, 3 and 4, the total injection flow rate was allowed to fluctuate with different pulse durations (τ =3,10,6 minutes, respectively) of equal amplitude. In order to minimize experimental disturbances during injection, we use two connected sets of syringes to rapidly extract and replace the fluids contained in the inflow reservoir of the tank (with a transient of roughly 4 seconds). Fluctuations were created by two programmable peristaltic pumps connected in parallel. One to maintain the minimum flow rate and the other to create intermittent pulses (Figure3.2). As a result, during experiments 2, 3 and 4, flow fluctuations produced an intermittent hydraulic head difference between the inflow and outflow reservoirs that varied between 1.4 cm and 0.8 cm, obtained respectively during the injection of the maximum and minimum total flow rate.

Table 3.2: Experimental flow and tracer conditions

Parameter	**Symbol**	**Units**	**Exp.1**	**Exp.2**	**Exp.3**	**Exp.4**
Rhodamine B concentration	C_0	mg/L	200	200	200	200
Injected Volume	V_{inj}	mL	4464	4464	4464	4464
Injected Time	T_o	min	62	63	61.5	60
Maximun total flow rate	Q_{inj}^{max}	mL/min	72	96	96	96
Minimun total flow rate	Q_{inj}^{min}	mL/min	72	48	48	48
Pulse duration	τ	min	constant	3	10	6

In order to measure depth-average flux concentration breakthrough curves of Rhodomine at the tank outlet, we connected the outflow chamber to a high-precision fluorimeter ($GGUN - FL22, UNINE$), which automatically took measures every 10 seconds. This fluorimeter can measure concentrations between 0.1 ppb to 1 ppm. Since the injected concentration of Rhodamine is 200 ppm, it was necessary to use a different instrument to measure the concentrations above 1 ppm. To do this, we took 5 mL samples of fluid at the tank outlet every 1.5 minutes. These samples were afterwards diluted in the laboratory and measured with a fluorimeter ($Aquafluor, TurnerDesing$).

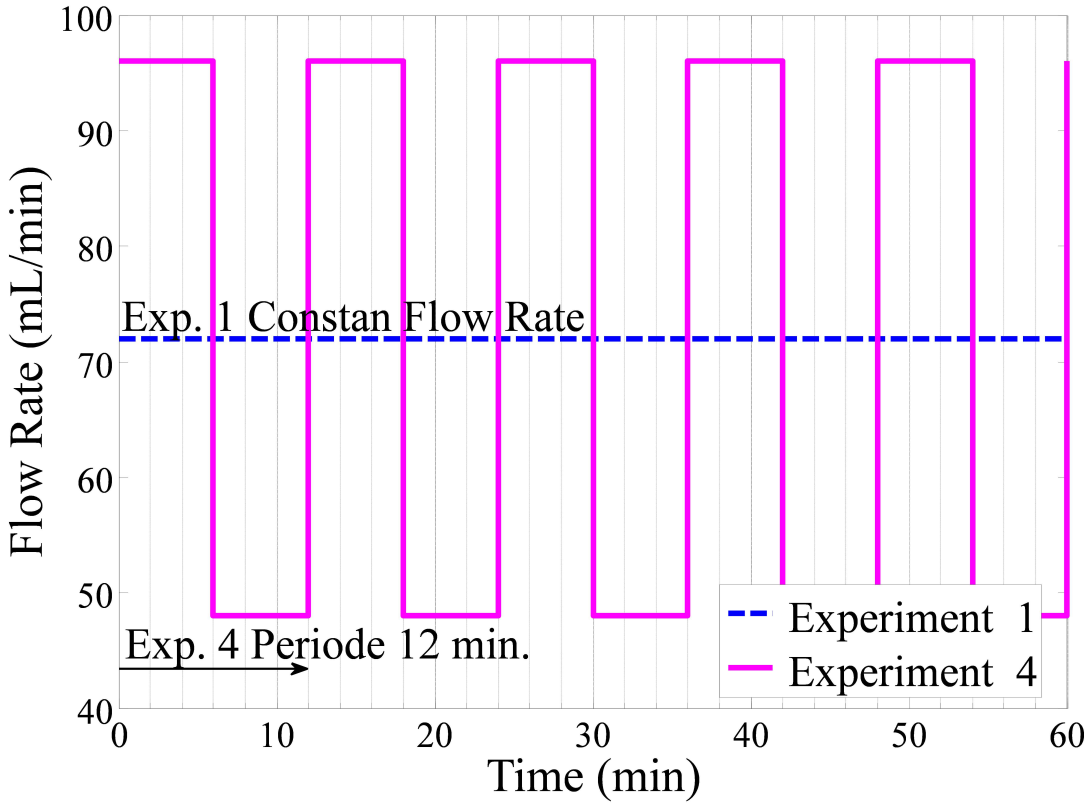

Figure 3.2: Illustration of the flow fluctuation function used during experiment 1 (steady-state flow conditions) and 4 (with a pulse duration of 6 minutes)

3.2.3 Image acquisition and image processing

The plexiglass structure of the sand box permits the visualization of the optical tracer transport without disturbing the mixing dynamics occurring inside the aquifer. Many authors have utilized optical tracers to visualize and quantify concentrations in synthetic aquifers. We choose reflected light techniques for image analysis so as to analyze typical (non-transparent) sand material. We tested four different types of light sources: incandescent, halogen, fluorescent and LEDs. Best results in terms of sensitivity, temperature and fluctuations were obtained with LEDs. Thus, two LED lights were placed at a distance of 20 cm from the tank. A CCD camera ($AVTGuppyF-080B/C$) was used to continuously record the red (R), green (G), and blue (B) color images of the tracer experiment. A computer program ($AVTSmartViewv1.7.2$) controls the image acquisition and the transfer of information into a computer. We set all parameters manually (relative aperture F5.6, shutter speed 1/30). These parameters are the same for both calibration and image processing of the four experiments. Images were acquired every 6 seconds both during Rhodamine injection and flushing. The camera and the tank are fixed to a metal structure that is placed inside a black room to fully control the light intensity emitted to and reflected from the tank. The black room is located inside a temperature controlled lab, ventilated with fans to ensure a constant temperature. The spatial resolution of the camera is 1024×728 pixels; each pixel represents an area of 0.32×0.32

mm^2 and has a color resolution of 8 bits. Thus, the RGB color channels range linearly between 0 to 255 in terms of light intensity. The concentration interpretation of optical tracers is based on the relationship between light intensity and tracer concentration. The application of such relationship in porous media can be cumbersome because light intensity is affected by factors other than absorption and reflection of a light ray passing through a fluid with tracer concentrations. Grain borders, light intensity fluctuations and non-uniform brightness contribute to generate noise in the images. Here, we use a locally adapted kernel regression technique specifically designed to optimally reconstruct concentrations from noisy RGB images. Image processing details can be found in (Castro-Alcalá et al., 2012). This methodology is capable of providing optimal images of both concentration and mixing of high quality in complex porous systems.

3.3 Interpretacion Methods

3.3.1 Effective porosity

Effective porosity is generally defined for solute transport as that portion of the soil or rock through which chemicals move, or that portion of the media that contributes to flow (Fetter, 1993; Domenico, 1990; R. et al., 1987) added some confusion by defining effective porosity as that part of the pore space where velocity is greater than the average fluid velocity. However, its in simplest and traditional form, effective porosity n_e is

$$\phi_e = \frac{q}{v} \tag{3.3}$$

where v is the mean velocity of a conservative tracer and q is the specific discharge, or Darcy velocity (e.g.,Bear (1988)). It is well recognized that effective porosity is less than the total porosity, because, even if the medium is fully saturated, not all of the water- filled pores are interconnected or contribute to flow. Therefore, terms such as mobile and immobile water or dead-end pores are also used in reference to the definition of effective porosity.

3.3.2 Kube Number

A dimensionless quantity, the Kubo number Î°, is defined so as to measure the capacity of the trajectories to explore the space structure of the stochastic velocity field before the latter changes due to flow fluctuations (Dentz and Carrera, 2005). The Kubo number compares the average transported distance of a solute during the correlation time of the flow fluctuations with the correlation length of the natural log of hydraulic conductivity. It represents a measure of the solute's capacity for exploring the space structure of the velocity field before the latter changes. In mathematical terms, this Kubo number determines the importance of the Lagrangian nonlinearity introduced in flow equation by the space dependence of the velocity field (Dentz and Carrera, 2005). Importantly, (Dentz and Carrera, 2005) theoretically demonstrated in stochastic hydraulic conductivity fields that the effects of temporal fluctuations on the solute plume behavior are most significant when the kubo number is close to one. In this regime, the effective transverse dispersivity is maximized. Here, the Kubo number k is defined as

$$k = \frac{v\tau}{\ell_x} \tag{3.4}$$

where v is the mean velocity of the solute plume (non-reactive), τ is the pulse duration of the flow fluctuations, and ℓ_x is the longitudinal average size of individual fine sand lenses. Note that

this kubo number is adapted (but not equal) from (Dentz and Carrera, 2005) so as to consider a deterministic pulse wave flow fluctuation that is not random in nature.

3.3.3 Conceptual transport models

Two conceptual transport models were used to interpret transport behavior. The effective advection-dispersion equation (ADE) and the multirate mass transfer model (MRMT). The first one is used to estimate apparent dispersion coefficients and the other is used to characterize tailing behavior of the concentration breakthrough curves and immobile porosities. We briefly describe these models in the following sections.

3.3.3.1 The effective advection-dispersion equation

The usual continuum approach to solute transport in porous media invokes the use of concentrations as representative average quantities of solute occurring in the pore fluid within a finite representative elementary volume of the porous medium (Bear, 1972). Associating this mean value with its centroid results in the requisite function of concentrations, which is now continuously differentiable in space. This volume average concentration is usually denoted as resident concentration, $c_r(x,z,t)$. The advection dispersion equation is typically use to describe nonreactive transport at the local scale (at any given point of the tank),

$$\phi\frac{\partial c_r}{\partial t} = -\nabla\cdot(\mathbf{q}c_r) + \nabla\cdot(\phi\mathbf{D}\nabla c_r) \tag{3.5}$$

Here, in order to effectively model the evolution of solute concentrations during the tracer experiments, we described transport behavior as a whole by looking at the depth-average concentration, defined as

$$\bar{c}_r(x,t) = \frac{1}{h}\int_o^h c_r(x,z,t)dz \tag{3.6}$$

Where h is the saturated thickness of the tank. Assuming that hydrodynamic dispersion can also be described by Fick's law at the scale of the experiment, the mass balance of $\bar{c}_r$ can be written as

$$\frac{\partial \bar{c}_r}{\partial t} = -v\frac{\partial \bar{c}_r}{\partial x} + D\frac{\partial^2 \bar{c}_r}{\partial x^2} \tag{3.7}$$

where q is the mean flux ($q = Q/A$), ϕ is the porosity (assumed constant), and D_a is an apparent dispersion coefficient. The volume-average theory (Wood et al., 2003) or stochastic theories (Gelhar, 1993; Dagan, 1989) demonstrate the validity of this effective transport model under certain limiting conditions. The solution of this effective ADE depends on the initial and boundary conditions. For a semi-infinite system, the following boundary conditions are typically used,

$$\frac{\partial \bar{c}_r}{\partial x} = (\infty, t) = 0 \tag{3.8}$$

$$\left(\bar{c}_r - \frac{D}{v}\frac{\partial \bar{c}_r}{\partial x}\right)\Bigg|_{x=0^+} = C_0 \quad for \quad 0 < t \leq t_0 \tag{3.9}$$

$$\left(\bar{c}_r - \frac{D}{v}\frac{\partial \bar{c}_r}{\partial x}\right)\Bigg|_{x=0^+} = 0 \quad for \quad 0 < t \leq t_0 \tag{3.10}$$

where v is the average flow velocity at the x location, i.e., $v = q/\phi$. The solution of the ADE subject to this boundary conditions has been given by (Lindstrom et al., 1967),

$$\bar{c}_r(x,t) = C_0 A(x,t), \quad for \quad 0 < t \leq t_0 \tag{3.11}$$

$$\bar{c}_r(x,t) = C_0 A(x,t) - C_0 A(x,t-t_0), \quad for \quad t > t_0 \tag{3.12}$$

Where

$$\begin{aligned} A(x,t) &= \frac{1}{2} erfc\left[\frac{x-vt}{2(Dt)^{1/2}}\right] + \left[\frac{v^2 t}{\pi D}\right]^{1/2} exp\left[\frac{-(x-vt)^2}{4Dt}\right] \\ &\quad - \frac{1}{2}\left(1 + \frac{vx}{D} + \frac{v^2 t}{D}\right) exp\left(\frac{vx}{D}\right) erfc\left[\frac{x-vt}{2(Dt)^{1/2}}\right] \end{aligned} \tag{3.13}$$

In many cases, flux concentrations rather than volume-average concentrations may be of primary interest. In our experiments, both flux and resident concentrations are measured. Flux concentrations are measured at the outlet of the tank since we sampled the solute after passing through the end of the aquifer surface. On the contrary, the maps of concentrations obtained from image analysis gives the resident concentrations (at any given point of the aquifer). The relationship between flux and resident concentrations was derived by (Kreft and Zuber, 1978; Parker and Genuchten, 1984),

$$\bar{c}_f = \bar{c}_r - \frac{D}{v}\frac{\partial \bar{c}_r}{\partial x} \tag{3.14}$$

which is valid for nonzero water velocities. Flux concentrations may be interpreted physically as representing the mean of the microscopic fluid concentrations weighted by their respective microscopic fluid velocities. The discrepancy between $\bar{c}_f$ and $\bar{c}_r$ increases with the apparent dispersivity or mixing. In the special case of $v = 0$ with mixing solely by diffusion, $\bar{c}_f$, has no physical relevance and is mathematically undefined. The solution of the ADE for flux concentrations is (Parker and Genuchten, 1984)

$$\bar{c}_f(x,t) = C_0 B(x,t), \quad for \quad 0 < t \leq t_0 \tag{3.15}$$

$$\bar{c}_f(x,t) = C_0 B(x,t) - C_0 B(x,t-t_0), \quad for \quad t > t_0 \tag{3.16}$$

Where

$$B(x,t) = \frac{1}{2} erfc\left[\frac{x-vt}{2(Dt)^{1/2}}\right] + \frac{1}{2} exp\left(\frac{vx}{D}\right) erfc\left[\frac{x-vt}{2(Dt)^{1/2}}\right] \tag{3.17}$$

3.3.3.2 The Multirate MAss Transfer Model

The effective ADE model assumes that solute transport can be depicted as a Fickian process at the macroscale. This often contradicts field and laboratory observation of non-Fickian or anomalous transport (e.g., Berkowitz et al. (2006)). These observations have motivated intense research efforts towards alternative effective transport models. In this context, here we used the multirate mass transfer model (MRMT), proposed by (Haggerty and Gorelick, 1995), that conceptualizes the

system as a multiple continuum formed by a mobile domain and any number of immobile domains. Mass transfer between the former and any one of the latter is characterized by a given mass transfer coefficient, α. This transport model has been shown to successfully reproduce the late-time behavior of the concentration breakthrough curves. Mathematically, the MRMT model is described by the following mass balance equation,

$$\frac{\partial \bar{c}_m}{\partial t} + \beta \int_0^\infty p(\alpha) \frac{\partial \bar{c}_{im}(\alpha)}{\partial t} d\alpha = -v_m \frac{\bar{c}_m}{\partial x} + a_l v_m \frac{\partial^2 \bar{c}_m}{\partial x^2} \tag{3.18}$$

where $\bar{c}_m$ is the depth-average concentration associated with the mobile domain, $\bar{c}_{im}(\alpha)$ is the depth-average concentration in the α-immobile domain, a_l is the longitudinal dispersivity, $p(\alpha)$ is the probability density function of mass transfer rates, v_m is the mean groundwater velocity in the mobile domain, and β is the mass transfer capacity, defined as the ratio between immobile and mobile porosity,

$$\beta = \frac{\phi_{im}}{\phi m} v_m = \frac{q}{\phi m} \tag{3.19}$$

where ϕ_m is the porosity of the mobile domain, and ϕ_{im} is the total porosity of the immobile domain (sum of all individual immobile porosities). By continuity, the sum of mobile and immobile porosity must be equal to the total porosity, $\phi = \phi_m + \phi_{im}$. The mass transfer equations needed to close the system are given as

$$\frac{\partial \bar{c}_m(\alpha)}{\partial t} = \alpha(\bar{c}_m - \bar{c}_{im}(\alpha)), \quad \forall \alpha \tag{3.20}$$

where α is a lumped mass transfer coefficient that includes the effects of diffusion and other mass transfer processes. It is important to note here that the concept of mobile porosity is similar to that of effective porosity. From this, in this work, we will consider that $\phi_m \approx \phi_e$. Note also that this model is mathematically equivalent to consider a simple mass transfer coefficient that varies in time (Fernaàndez-Garcia and Sanchez-Vila, 2015).

Different MRMT models can be found in the literature. Such models are defined in terms of the probability density function of mass transfer rates or the corresponding memory function (Carrera et al., 1998). Among them, the often observed power law tailing behavior in BTCs has favored the use of the truncated power-law memory function (e.g., Haggerty et al. (1998); Fernàndez-Garcia et al. (2009); Pedretti et al. (2013)). In this case, the probability density function of mass transfer rates is

$$p(\alpha) = A_1(k) I(\alpha) \alpha^{m-3}, \quad m > 0, \tag{3.21}$$

where $I(\alpha)$ is an indicator function that is equal to one when $\alpha_{min} \leq \alpha \leq \alpha_{max}$ and zero otherwise, and $A_1(m)$ is a constant value that normalizes the probability density function to integrate to unity,

$$A_1(m) = \{ \frac{m-2}{\alpha_{max}^{m-2} - \alpha_{min}^{m-2}} \quad if \quad m \neq 2 \frac{1}{ln\left(\frac{\alpha_{max}}{\alpha_{min}}\right)} \quad if \quad m = 2 \tag{3.22}$$

The solution of the governing equations of the MRMT model is known in the Laplace space (Haggerty and Gorelick, 1995), and can be easily simulated with the STAMMT-L code (Haggerty and Reeves, 2002) through numerical inversion of the Laplace transform solution. This code allows the immobile zone to be represented as a diffusive domain of prescribed geometry and dimension-

ality. It also allows the immobile zone to have either a single value or a distribution of diffusion rate coefficients or first-order mass-transfer rates, which may be interpreted as variability in either the apparent diffusion coefficient, matrix block size, or both. The truncated power law model is also implemented.

3.4 Results

3.4.1 Temporal Evolution of resident concentrations

Our experiments suggest that the cumulative effects of heterogeneity and temporal flow fluctuations on transport are complex. Figure 3.3 presents a sequence of the sand box images taken at selected times during the experiment and processed afterwards into concentration maps. Here, concentrations have been normalized by the injected concentration, C_0. Results show that the solute plume obtained with flow fluctuations is radically different from the tracer solution obtained under steady-state flow. This must be attributed to the nonlinear dependence of transport concentrations on flux. In our case, when velocity fluctuates, the bulk of plume advances faster through the top portion (which contains few low permeability inclusions) than through the bottom portion (which contains many fine sand inclusions). This is surprising because velocity through the high permeability zones should be independent of whether they are surrounded by zones of low permeability, which is just what happens for the steady-state flow experiment. We attribute this difference to diffusivity, which is non local, so that pressure fluctuations are transmitted much faster through areas where most of the medium displays high permeability. Other possible explanation for this observation might be that the raising heads in unconfined aquifers changes the transport connectivity structure or cause an expansion of the medium that leads to an increased permeability that is not compensated by the corresponding contraction when heads fall, yet another consequence of the non-linear dependence of transport on flow.

Moreover, the relationship between heterogeneity and flow fluctuations is seen complex. Fluctuations not only affect solute transport in high permeability regions (top) but seem to also increase the accessibility of the solute tracer to the fine sand material. Figure 3.3 shows that, with flow fluctuations, a large part of the solute tracer is still trapped in the low permeability inclusions during water flushing. Since more mass enters into the low permeability regions with flow fluctuations, tracer extraction by water flushing becomes a more difficult task. Interestingly, fluctuations seem also to develop fewer solute plume fringes of larger transverse size compared to the steady-state flow experiment.

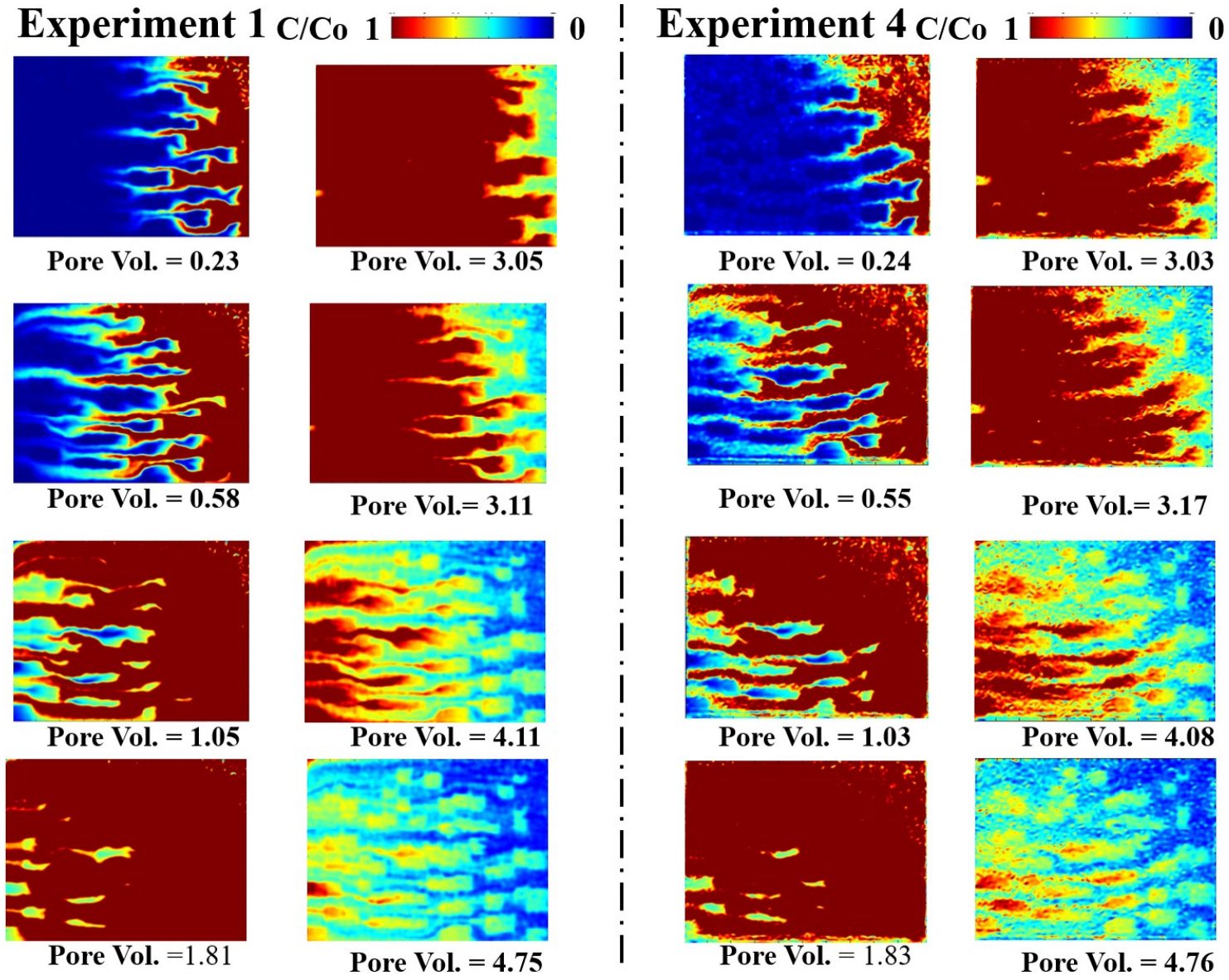

Figure 3.3: Sequence of the sand box images taken at selected times during the course of the experiments 1 and 4, and processed into concentration maps.

3.4.2 Behavior of breakthrough curves

The effect of temporal flow fluctuations on the resulting concentration breakthrough curves (BTCs) is shown in Figure 3.4. To compare experiments, the elapsed time from the injection of the tracer is given in terms of pore volumes, defined as the ratio of the injected water volume at a given time to the total water volume in the aquifer. In spite of the fast advance of the tracer plume nearby the water table, fluctuations cause an overall delay of the early arrival of the BTC. We attribute this delay to the fact that the leading edges of the tracer plume, corresponding to the fastest flow lines, become blurred by fluctuations due to an enhancement of transverse mixing. The net effect is an increase in the effective mobile porosity. Flow fluctuations increase the fraction of the sampled porous media that is directly accessed by the injected solute. Notice, for instance, that the transverse size of the preferential paths produced with temporal flow fluctuations is significantly larger than that observed under steady-state flow conditions. These effects are seen more pronounced in experiments 3 and 4, which are characterized by a kubo number close to or larger than one; the time scale of fluctuations is smaller than the time scale of advection. Contrary, these effects are seen negligible in experiment 2 where the kubo number is significantly smaller than one. This illustrates the strong interplay between the time scale of fluctuations and advection, which is demonstrated to be controlled by the kubo number.

Surprisingly, the late-time behavior of the concentration BTC does not change substantially with flow fluctuations, i.e., the distribution of the depth-integrated concentrations measured at the tank outlet follows always a power law behavior with $\bar{c}_f \sim t^{-2.1}$, no matter the type of flow fluctuation applied. It is well known that heterogeneity (i.e., the spatial variability in the hydraulic conductivity) can produce a power law behavior in the BTC (Levy and Berkowitz, 2003; Willmann et al., 2008; Riva et al., 2008; Henri and Fernàndez-Garcia, 2014). The exponent of the power law is usually denoted simply as the slope since a log-log plot of the concentration BTC displays a straight line at late times. Our results agree with the slopes reported in the literature that range between 1 and 3 (Becker and Shapiro, 2000; Mckenna et al., 2001; Pedretti et al., 2013). Several processes can develop tailing in the BTC. At the local scale, Zinn et al. (2004) have experimentally shown that slow advection or diffusive mass transfer from low permeability inclusions can produce tailing, typically dominated by the fastest process. In our case, slow advection is clearly the dominant process, i.e., the time needed for the solute to diffuse out of the fine sand inclusions is about 17 days whereas the time needed to transport solute by advection across an inclusion is about 23 minutes (in average sense). This is also visually manifested in Figure 3.3 which shows a clear advective front inside the inclusions. On the other hand, at a larger scale, it has been numerically and experimentally demonstrated that the late-time distribution of depth-average breakthrough curves in heterogeneous hydraulic conductivity fields is mainly controlled by the stratification of the solute tracer (Pedretti et al., 2013). In this case, the tail develops as a superposition of individual breakthrough curves resulting from different portions of the tracer mass. Interestingly, our results indicate that stratification is also important in this case. Flow fluctuations cannot substantially change the stratification of solute pathways and therefore the slope is not affected by flow fluctuations.

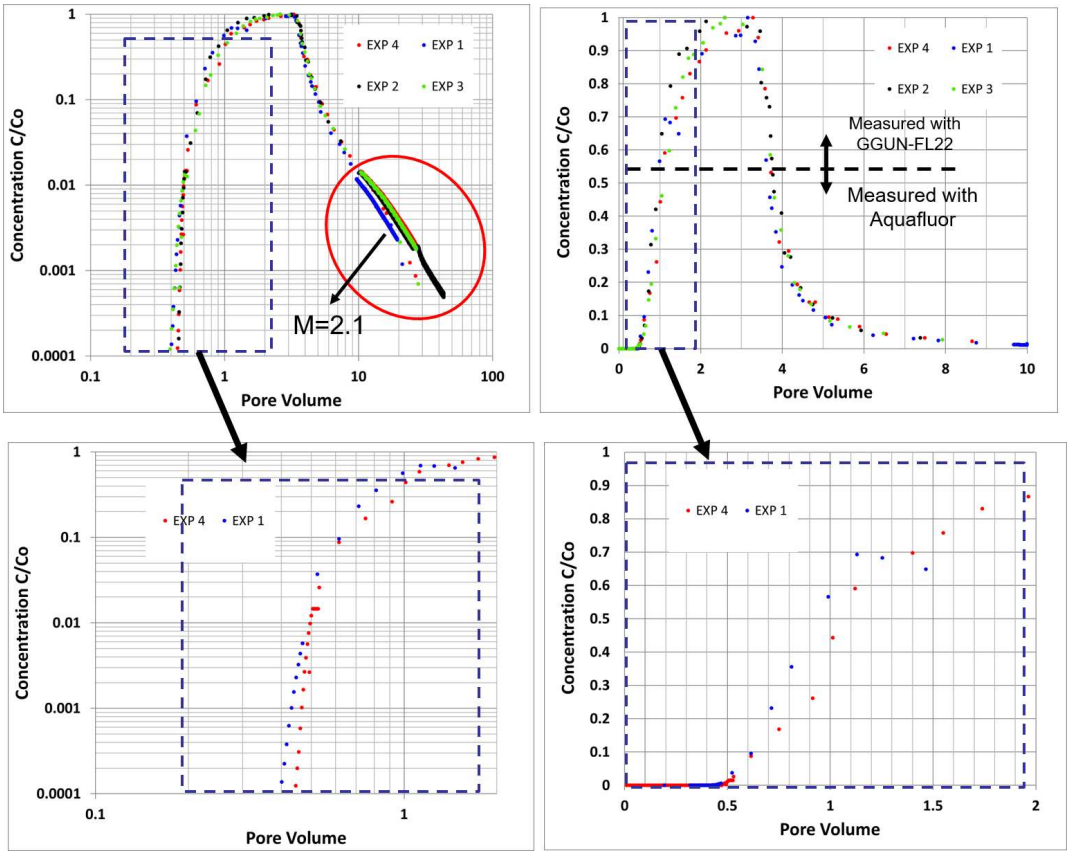

Figure 3.4: Comparison of tracer breakthrough curves obtained with and without flow fluctuations

3.4.3 Effect on macrodispersion, local dispersion and mixing

We estimate different dispersion parameters by fitting the effective ADE transport model to the experimental data in different ways. Resulting parameters have different meanings in terms of mixing and spreading. Firstly, we fitted depth-average concentrations, obtained by vertical integration of the concentration maps previously determined by image processing, to the corresponding solution of the effective ADE for resident concentrations. The apparent dispersion coefficient obtained this way describes the total spreading of the solute plume in the direction of the mean flow. The longitudinal distribution of the depth-average concentration is a smooth function of concentrations as it averages regions with high and low solute concentrations in the vertical direction. It is therefore a larger value than the local dispersion (components in $\mathbf{D}$). This parameter is not controlled by the solute mixing processes occurring at the fringes of the solute plume (at the local scale) but gives a general measure of longitudinal dispersion caused by the different velocities of the plume fringes. We denote this parameter estimate as longitudinal macrodisperison D_{macro}. The best fit between depth-average experimental resident concentrations for experiments 1, 2, 3 and 4 and modeling results is shown in Figure 3.5. To calibrate the parameters of the effective ADE, we considered only two adjustable parameters v and A_{macro}, where $A_{macro} = D_{macro}/v$. Calibration is performed manually against the data.

Another interesting measure of dispersion was obtained by fitting the tracer BTCs measured at

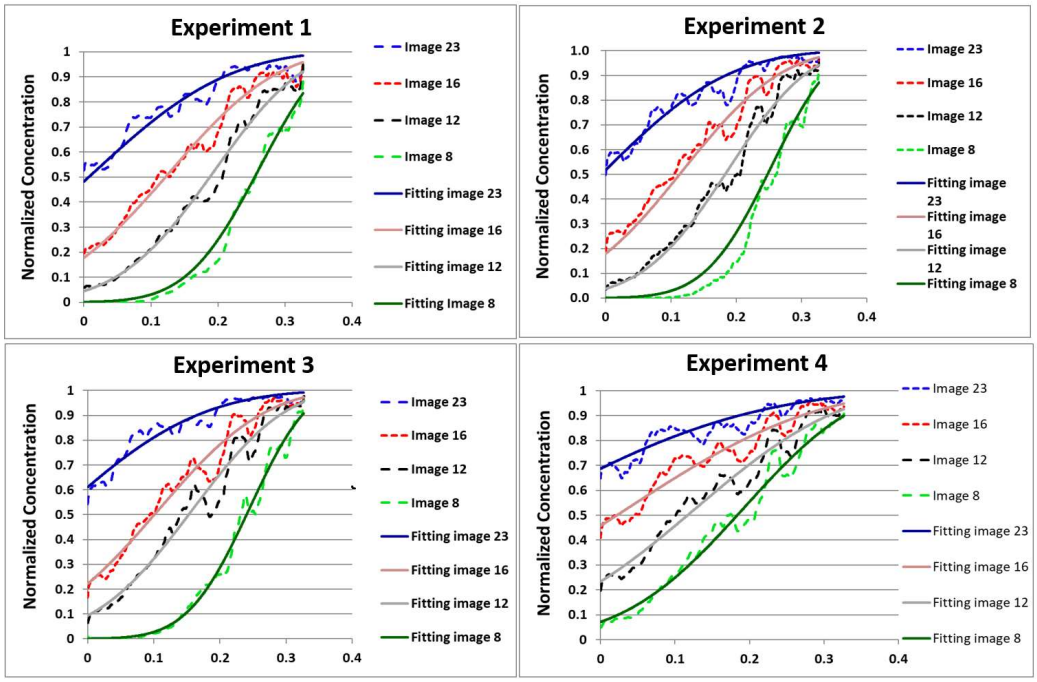

Figure 3.5: Best fit between experimental data (depth resident concentrations) and the effective ADE model

the tank outlet with the analytical solution of the effective ADE for flux concentrations. In this case, since tailing prevents a good fit of the whole BTC, we concentrate the analysis on the early arrival, defined here as the rising limb of the concentrations below 1% of C_0. Calibration is performed by minimizing the sum of square errors of these early arrival concentrations. This dispersion parameter does not capture the variability in the plume fringe velocities but provides a measure of the local dispersion associated with the fastest fringe. This parameter is therefore related to local mixing and not to longitudinal macrodispersion. We denote this parameter as D_{local}. Its corresponding dispersivity coefficient, referred to as A_{local}, provides a measure of the size of the mixing zone in the mean flow direction. The best fit between tracer BTCs for experiments 1, 2, 3 and 4 and modeling results is shown in Figure 3.6 (black line).

The calibrated transport parameters are summarized in 3.3. Results point out that the effective size of the mixing zone characterized by the local longitudinal dispersivity A_{local} is significantly reduced due to flow fluctuations. In fact, we observed that A_{local} changes from 0.37 cm (steady-state flow case) to 0.07 cm when flow fluctuations are applied with $\tau = 6$ and a kubo number close to 1. Invoking local mass conservation, this indicates that local transverse dispersivity/mixing is substantially enhanced due to flow fluctuations. This agrees with our previous observation derived from the temporal evolution of resident concentrations, i.e., the transverse size of the solute fringes produced by flow fluctuations is visually larger. At the same time, results show that flow fluctuations can enhance longitudinal macrodispersion. An effect that is seen to be controlled by the kubo number. (Dentz and Carrera, 2005) theoretically demonstrated in stochastic hydraulic conductivity fields that the effects of temporal fluctuations on the solute plume behavior are most significant when the kubo number is equal to one. Our results provide experimental evidence of these results. Most likely, in this case, macrodispersion seems to increase with fluctuations because a larger portion of the solute plume is transferred to the plume front due to an increase in mobile porosity, at the same time that more mass enters into low permeability inclusions due to an enhancement of transverse dispersivity (and gets trapped). These experimental observations contradict the numerical simulations presented by (De Dreuzy et al., 2012a) who suggested that transverse temporal flow fluctuations can increase the mass exchange between the mean flow pathways, decelerating the plume front and accelerating the plume tail. We finally acknowledge that, in principal, the flow fluctuations induced in the tank will mainly produce longitudinal flow fluctuations. However, the fact that the experimental aquifer constitutes a free aquifer may have generated additional vertical flow fluctuations driven by the variations of the water table.

Table 3.3: Transport parameters calibrated against experimental data using the effective ADE model; Macrodispersivity is obtained from depth-average resident concentrations and local dispersivity from the early arrival of breakthrough curves.

Parameter	**Symbol**	**Units**	**Exp.1**	**Exp.2**	**Exp.3**	**Exp.4**
Pulse duration	τ	min	Steady	3	10	6
Kubo number	k	-	-	0.49	1.72	0.99
Solute mean velocity	v	cm/min	0.76	0.76	0.81	0.78
Macrodispersivity	A_{macro}	cm	4.42	3.75	3.81	6.19
Local dispersivity	A_{local}	cm	0.32	0.14	0.28	0.07

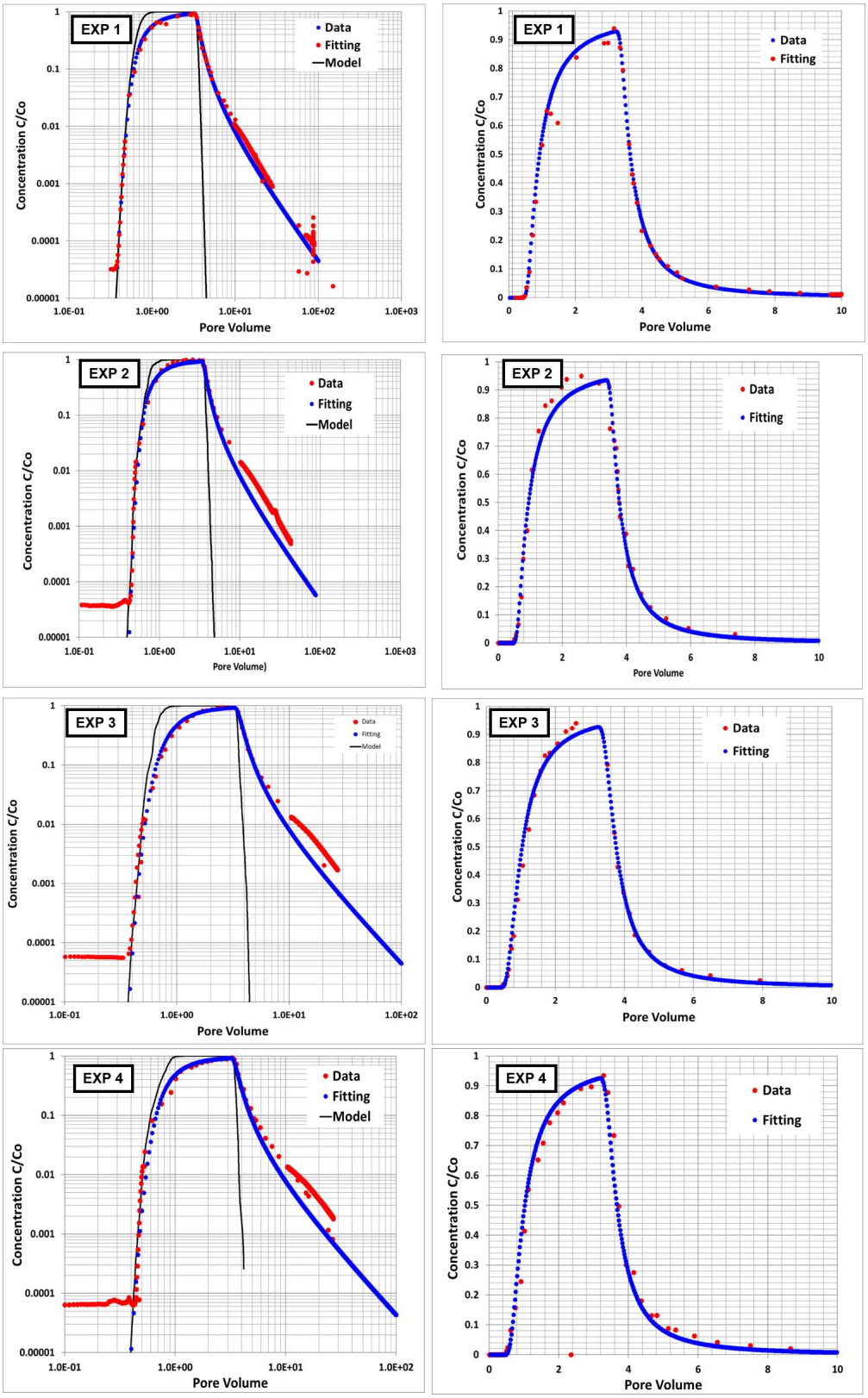

Figure 3.6: Best fit between experimental tracer breakthrough curves measured at the tank outlet (red) with the effective ADE model (black line) and the MRMT model (blue).

3.4.4 Effect on macrodispersion, local dispersion and mixing

The measured tracer BTCs were also used also to estimate the MRMT model parameters. In this case, the MRMT model is capable to fit the entire BTC, including the late-time behavior (tailing) with the truncated power law model. To calibrate the parameters of the MRMT model, we consider four adjustable parameters, a_l, v_m, β, and α_{max}. The slope of the breakthrough curve m was fixed from direct observation of the late-time behavior of the breakthrough curve. Note that (Haggerty et al., 1998) demonstrated that the MRMT models yields BTCs that behave as a power law at late times ($c \sim t^{-m}$) when $p(\alpha)$ follows a truncated power law model ($p \sim \alpha^{m-3}$). Also, $\alpha_m in$ is seen insensitive to calibration and it is therefore fixed to $\alpha_m in = 10^(-5)$. Calibration is performed manually against the data associated with tracer BTCs measured at the tank outlet.

Table 3.4: Transport parameters calibrated against experimental data (tracer breakthrough curves measured at the tank outlet) using the MRMT model with a truncated power-law probability density function of mass transfer rates

Parameter	Symbol	Units	Exp.1	Exp.2	Exp.3	Exp.4
Pulse duration	τ	min	Steady	3	10	6
Kubo number	k	-	-	0.49	1.72	0.99
Longitudinal dispersivity	a_l	cm	8.7	0.52	0.9	0.9
Mobile velocity	v_m	cm/min	1.64	1.54	1.65	1.52
Mass tranfer capacity	β	-	3.5	3.22	3.52	3.17
Mobil porosity	ϕ_m	-	0.089	0.095	0.089	0.096
Immobil posority	ϕ_{im}	-	0.311	0.305	0.311	0.304
Slope of BTC	m	-	~ 2	~ 2	~ 2	~ 2
Minimum mass transfer coefficient	α_{min}	min^{-1}	0.00001	0.00001	0.00001	0.00001
Maximum mass transfer coefficient	A_{max}	min^{-1}	12	7	15	10

The best fit between experimental observations (experiments 1, 2, 3 and 4) and modeling results is shown in Figure 3.6 (Black line called Model). The fitting parameters are presented in Table 3.4. We can see that values of mass transfer capacity $\beta = \phi_{im}/\phi_m$ decrease with flow fluctuations, meaning that mobile porosity increase with fluctuations. Compared to the steady-state flow experiment, the effective mobile porosity is increased by an 8 percent when the kubo number is close to 1. Mobile porosity is easily determined by the relationship

$$\phi = \phi_m(1 + \beta) \tag{3.23}$$

This corroborates our previous conjecture; flow fluctuations are capable to enhance the accessibility of the solute tracer in low permeability regions. In addition, the largest mass transfer coefficient α_{max} is seen to increase with flow fluctuations, suggesting also that the size of the immobile region has become smaller.

3.4.5 Conclusion

We have performed tracer experiments to evaluate the effect of flow fluctuations on solute transport behavior in a heterogeneous aquifer system reconstructed in the laboratory under controlled conditions. Aquifer heterogeneity consists of low permeability fine sand inclusions of different sizes

embedded in an otherwise coarse material of high permeability. We have compared the tracer solution obtained with steady-state flow with those obtained applying different flow fluctuations characterized by a symmetric square wave function. The tracer experiments involve three different pulse durations. Experimental data include tracer breakthrough curves at the tank outlet and high-resolution images of the temporal evolution of the tracer obtained with a CCD camera. Data interpretation is based on visual inspection of the concentration images and breakthroughs as well as on the inference of apparent transport parameters calibrated against data with different conceptual models to quantify macrodispersion, mixing, mobile/immobile porosity and mass transfer coefficients. Experimental results indicate that the mean solute plume obtained with flow fluctuations is radically different from that obtained with steady-state flow conditions. Flow fluctuations generate fewer solute plume fringes with large transverse sizes. Fluctuations seem to also increase the accessibility of the solute tracer to the fine sand material, causing the entrapment of a large part of the solute tracer in low permeability inclusions. These processes did not affect the late-time behavior of the depth-average breakthrough curves measured at the tank outlet, showing always the same slope, because the aquifer stratification was not severely modified. Yet, a delay observed in the breakthrough curves due to flow fluctuations expressed a decrease in the effective velocity of the solute plume, which indicated an increase in mobile porosity. Combing this information with the changes observed in model parameters the following main conclusions are drawn: Flow fluctuations can enhance transverse mixing and mobile porosity. These phenomena transfer more mass to the plume front, which is now more mobile, and to the low permeability inclusions. As a result, the apparent longitudinal macrodispersion coefficient is substantially increased due to flow fluctuations. Importantly, these effects are seen to be controlled by the kubo number that relates the mean travel distance of the solute plume during a pulse duration with the average size of the low permeability inclusions. Experimental results determined that the effect of flow fluctuations is maximum (enhancement of transverse mixing and macrodispersion) when the kubo number is close to one.

Chapter 4

Heterogeneous Sand Box Experiments on the Impact Flux Fluctuations on the dynamics of the Mixing zone in Coastal Aquifers.

4.1 Introduction

Coastal aquifers are subject to intensive stresses in many coastal regions because they serve as major sources for the supply of fresh water (Werner et al., 2012). Understanding groundwater flow in coastal aquifers is essential for preventing seawater intrusion and assessing fresh groundwater reserves. It is also important for understanding submarine groundwater discharge and the fluxes of nutrients into the ocean (Burnett et al., 2006; MacCready and Geyer, 2010; Moore, 2010) Unfortunately, the study of coastal aquifers is complicated by the combined influences of (1) density variations, (2) heterogeneity (scale, shape or structure of the aquifer), and (3) temporal fluctuations of sea level and inland groundwater discharge. These produce complex hydrodynamic effects that effect the location, shape and extent of the dispersion zone (or mixing zone, wich in turn influences contaminant transport from the aquifer to the coastal sea and different chemical processes in the mixing zone.

Freshwater is lighter than seawater, so that it tends to float and discharge above a seawater wedge. One of the key issues in seawater intrusion (SWI) is to assess the penetration of this wedge. A rough approximation of the penetration can be obtained using the Ghyben-Herzberg approximation (actually derived by Du Commun (1828)), which assumes that seawater does not mix with freshwater and remains perfectly static (sharp interface approximation). This assumption has been widely used (see, e.g., Willis and Finney (1988); Emch and Yeh (1998); Naji et al. (1999); Cheng et al. (2000); Mantoglou et al. (2004); Park and Aral (2004); Reinelt (2005); QAHMAN et al. (2009); Park et al. (2009);. Actually, seawater and freshwater do mix, which causes seawater to flow inland and return to the sea along the mixing zone, thus forming a convection cell (Cooper, 1959). The loss of seawater pressure caused by this flux causes the interface to recede seawards, much as if the density contrast had been reduced (Pool and Carrera, 2011). Beyond its impact on SWI penetration, acknowledging mixing is also important for understanding reactions driven by mixing (Rezaeia et al., 2005; E. and F.; De Simoni et al., 2005; Garing et al., 2013).

While it is generally agreed that the mixing zone is critical for detailed understanding of SWI and bio-geo-chemical processes, the controls of its width and dynamics remain a subject of debate. Abarca et al. (2007) and Paster and Dagan (2008) argue that the width of the mixing zone is mainly controlled by transverse pore-scale dispersion, which yields a relatively narrow mixing zone. This would support the sharp interface approximation and is consistent with laboratory experiments performed in homogeneous media (Zhang et al., 2002; Volker, 2002; Goswami and Clement, 2007;

Abarca and Prabhakar Clement, 2009), but inconsistent with field observations, which often display broad (more than 10 m) mixing zones (Price et al., 2003; Langevin, 2003; Kim et al., 2007).

The disparity between field and theory has been attributed to heterogeneity and groundwater flow fluctuations driven by fluctuations of sea-level and/or inland discharge. Yet, stochastic (Dell'Oca et al., 2018), numerical simulations (Abarca et al., 2007) and laboratory experiments (Rahman et al., 2005a; Jose et al., 2004) conclude that heterogeneity does not cause a significant enhancement of transverse dispersion. Instead, SWI research has concentrated on the impact of fluctuations. (Li et al., 1999) showed that groundwater circulation and oscillating flows can greatly increase the rate of chemical transfer to the ocean. (Andersen, 2001) argued that water level fluctuations enhance the width of mixing zone and affect many chemical reactions.

(Moore, 1973), showed that beach rock cementation depends on the mixing of ocean and aquifer water. (Ataie-Ashtiani and Ketabchi, 2010) use a numerical model to show that tidal fluctuations forces the seawater to intrude further inland and create a thicker interface than would occur without tidal effects. These results contradict theoretical findings, which conclude that fluctuations do not cause dispersion in homogeneous media but simply cause plumes to be dragged back and forth without spreading (see discussion by de (De Dreuzy et al., 2012a), which is consistent with both numerical simulations and laboratory experiments (Kuan et al., 2012). (María et al., 2015) analyzed the joint effect of heterogeneity and groundwater flow fluctuations and concluded that, also contrary to the findings of (Ataie-Ashtiani and Ketabchi, 2010), the net effect of fluctuations in heterogeneous media is a displacement seawards of the SWI wedge, but that little effect was observed on the width of the mixing zone, which they attributed to the connectivity of 3D media, which led to relatively large values of hydraulic conductivity.

Actually,(Pool et al., 2014) showed that some mixing and spreading can be attributed to storativity, which causes sea-level fluctuations to be transmitted inland at a non-homogeneous rate.

An alternative explanation for broad mixing zones was proposed by (Lu and Luo, 2010), who showed that the movement of the mixing zone combined with kinetic mass transfer may widen the mixing zone. This would be consistent with the observations of (Castro-Alcalá et al., 2012), who found that mobile porosity is increased by fluctuations, which enhance transfer into " immobile " zones. Since kinetic mass transfer has also been widely used as a way of representing heterogeneity (see discussion by De Dreuzy et al. (2012c)), this finding suggests that it is the coupling of heterogeneity and fluctuations what causes broad mixing zones.

The conclusion of this long discussion is that most studies separate the impact of heterogeneity and temporally flow in the mixing zone. Results are contradictory, none of them really explains the observed wide mixing zones and none of them has been performed under controlled laboratory conditions. The objective of this work is to describe the results of laboratory experiments performed on a heterogeneous sand box to analyze the effect of groundwater flow fluctuations on the mixing zone, its dynamics, width and location.

4.2 Experimental procedure

A seawater intrusion experiment was conducted in a heterogeneous aquifer reconstructed in the laboratory using two types of sand with contrasting hydraulic conductivities. The objective of this particular distribution is to visualize and quantify the mixing dynamics occurring at the interface between two distinct materials with contrasting hydraulic properties.

4.2.1 Experimental Tank

The experiment was conducted in a quasi 2-D transparent $plexiglass^{TM}$ flow-through tank of length 34.7 cm, height 23.3 cm and width 2.5 cm. A conceptual diagram of the experimental setup is shown in Figure 4.1.

The flow tank consists of three principal sections: influent chamber, containing freshwater, effluent chamber, containing salt-water, and central flow chamber containing the porous medium. The influent and effluent chambers serve to prescribe head at the boundaries. To this end, water was pumped into either or both chambers by means of three high precision peristaltic pumps through a perforated vertical pipe driven into each chamber. These chambers are separated from the central chamber by a stainless steel mesh $US\#16$ that prevents porous medium grains from entering the influent and effluent chamber.

The central chamber was filled with a heterogeneous distribution of two types of sand: coarse, grain size from 1.0 to 1.2 mm, and fine, from 0.6 to 0.4 mm. The heterogeneity consists of 29 different rectangular inclusions of fine sand (low permeability) embedded in a matrix of highly permeable coarse sand (Figure 4.1). A 0.5 mm thick grid template of 20 columns was used to accurately emplace the sand by rows. Each row was saturated during sand emplacement to avoid air trapping and minimize segregation. The hydraulic conductivities of the two sand types were obtained using a constant head permeameter cell. The hydraulic conductivity was determined by taking the average of 5 individual constant head permeameter test. The resulting values were 1060 m/day and 67.5 m/day for the coarse and fine sand, respectively. The porosity was estimated gravimetrically as 0.4. A sieve analysis determined that the sand is poorly graded with a uniform coefficient of 1.2 and 1.25 for the coarse and fine sand, respectively. We argue that the permeability contrast between coarse and fine sands in our experiment is not particularly large. Silty clay layers can be expected adjacent to sand layers in coastal sedimentary settings (e.g.,Gamez et al. (2009))

4.2.2 Tracer Experiment

Halite (NaCl) was dissolved in deionizer-water with a concentration of 50 g/L to simulate the saltwater (the resulting density of 1037 kg/m^3 implies a buoyancy term gradient of 0.037). We added Rhodamine B (Panreac) with a concentration of 200 mg/l of saltwater to track the dense saltwater wedge by distinguishing the saltwater from ambient pore water. This compound neither adsorbs nor degrades in clean quartz sand and can therefore be considered as a conservative tracer. The actual saltwater intrusion experiment proceeded in two steps: generation of initial conditions and generation of response to fluctuations. In the first stage, Pump 3 (520S/R,Watson Marlow) injected a constant flow rate of 190 mL/min saltwater in the outflow chamber (Figure 4.1). Simultaneously, Pump 2 (323E/D,Watson Marlow) injected deionizer-water into the inflow chamber at the constant rate of 38 mL/min. Note that water level was maintained constant at the outflow chamber by means of an outflow spill, so that water flowed from the inflow to the outflow chamber even though the pumping rate into the inflow chamber was smaller than that at the inflow. This arrangement ensured that water below the spill was salty, which is important for seawater recirculation within the saltwater wedge (Simpson and Clement, 2003). Constant heads of 23.90 cm at the inflow chamber 1 and 23.0 cm at the outflow chamber (or an overall mean gradient is 0.9/34.7=0.026 m/m) were recorded during this stage, which lasted 4 hours. At this stage, colour at the intrusion wedge looked visually uniform, although, as we shall see, concentration turned out to be non-uniform after proper image processing. The second (fluctuations) stage was generated by (1) connecting Pump 1 (Ismatec) to Pump2, (2) reducing the injection rate of Pump 2 to a constant flow rate of 22 mL/min, and (3) letting Pump 1 fluctuate between 0 and 32 mL/min every 14 minutes (cycles

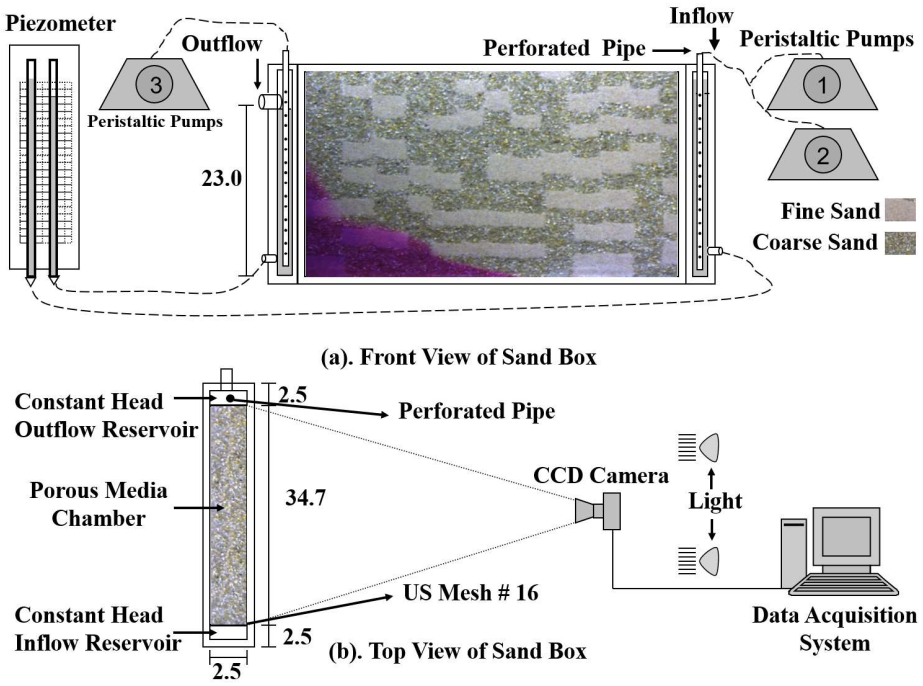

Figure 4.1: Schematic experimental setup of the sand box for seawater experiment.

of 28 min). This fluctuation produces cyclic head fluctuations between 23.30 cm and 24.30 cm at the inflow chamber.

4.2.3 Image acquisition and Image processing

To determine the concentration distribution across the fluctuating wedge during the experiment, we took photos with a charge-coupled device (CCD) camera ($AVTGuppyF - 080B/C$) every 6 seconds. The spatial resolution of the camera is 1024x728 pixels so that each pixel represents an area of 0.32 x0.32 mm^2 and has a color resolution of 8 bits per channel (red (R), green (G), and blue (B)), yielding a total bit range of 256 possible intensities (brightness values). A computer program $AVTSmartViewv1.7.2$ controls the camera settings and transfers the information to a computer. Camera settings were set manually (relative aperture F5.6, shutter speed 1/30). To provide even lighting on the tank, we use three LED (Light-Emitting Diode, 5500 °K) located 20 cm away from the tank. We constructed a metal structure to install the necessary accessories and fixing the camera and LED. A dark curtain placed around the entire metal structure prevented reflections and pollution by external light.

Image processing is a useful tool to obtain the spatial distribution of the solute concentration because, being non-intrusive, it does not disturb the flow field. The concept behind the procedure is that Rhodamine B reflects the variations of solute concentration through variations of color intensity represents the. That is, image analysis is used for obtaining concentration maps during the tracer test (Schincariol et al., 1993; McNeil et al., 2006; Goswami and Clement, 2007; Konz et al., 2008; Rahman et al., 2005a). While the concept appears simple, actual application is tricky because our sand box structure $plexiglass^{TM}$ is transparent, but the porous media consists of sand

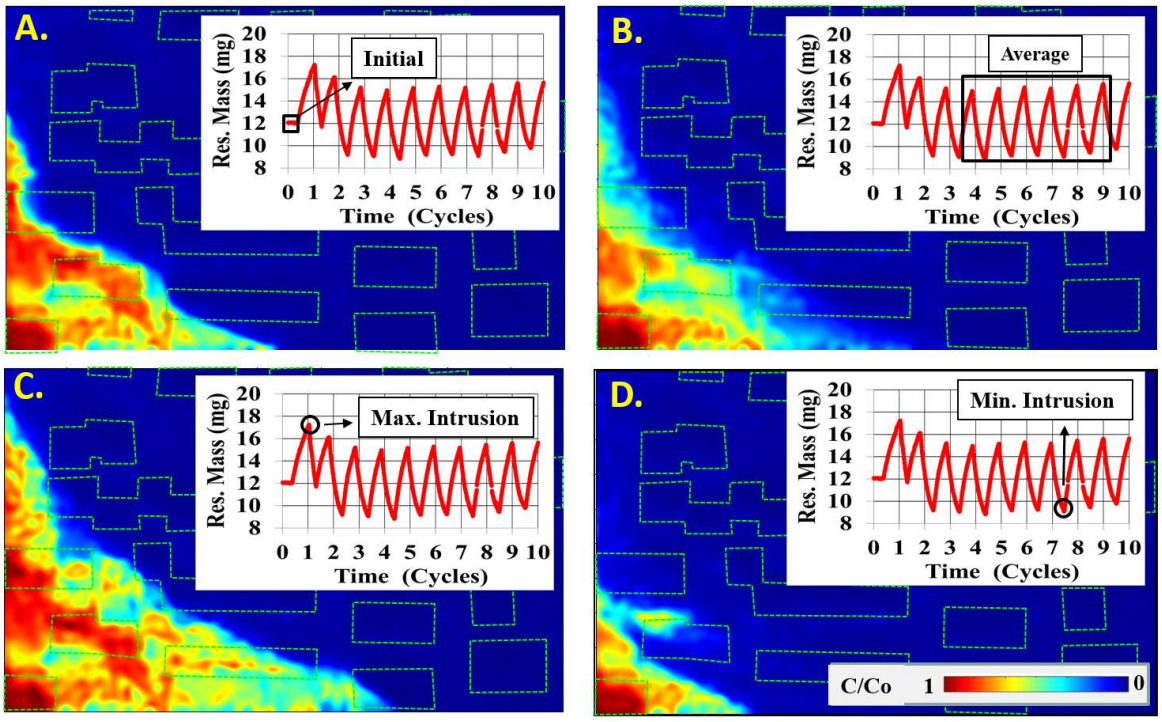

Figure 4.2: Behavior of seawater wedge for four different times. (A) S.S conditions; (B) Seawater wedge average for S.S fluctuation; (C) Maximum intrusion; (D) Minimum intrusion

with varying mineralogy, so that color intensity reflects not only concentration but other factors, such as fluctuations in the source light, brightness variations due to non-uniform lightning and the physical characteristic of the sand (color, roughness and geometrical properties. Therefore, if a fixed relationship is used, the resulting concentration maps tend to be noisy.

To address these problems, we followed the image-processing procedure of (Castro-Alcalá et al., 2012). First, the relationship between light intensity and concentrations was determined for each image pixel from pictures obtained with the sand box filled uniformly with 10 different concentrations of Rhodamine B (0, 10.33, 20.79, 30.21, 42.27, 105.87, 101.3, 150.67, 182.64, 210.2 mg/L). Each concentration was obtained by dilution with deionizer-water, starting from the initial saltwater with 210.2 mg/L. These relationships were used at every pixel to obtain concentrations from the pictures. The resulting concentration maps were still noisy. Therefore, we used a locally adapted kernel regression technique specifically designed to optimally smooth images described by (Castro-Alcalá et al., 2012) to reduce noise. This methodology is capable of providing optimal images of both concentration and mixing of high quality even at complex material edges between bodies of different sand.

4.3 Results and discussion

Results are summarized in Figure 4.2, which displays initial state, the average during the fluctuation stage, along with the maximum and minimum penetration. The first observation that emerges from Figure 4.2 is that the initial state is not really a steady state. Under steady state, salt water flux within the wedge would have eliminated fresh water inclusions. We did perform another experiment (not reported) starting with freshwater, but the result was further from steady state than the one displayed here. The fact that low salinity inclusions remain within the wedge steady discharge for a time equivalent to 8 cycles suggests that reaching a true steady state may take very long. This was known from homogeneous simulations (e.g.,Abarca et al. (2007); Pool et al. (2014)), but Figure 4.2 suggests that it may take longer under heterogeneous conditions. In fact, we find surprising that the low salinity inclusions do not occur at the low K regions, but below and to the left, i.e, upstream the low K regions with respect to the mean local salt water flux. This implies that these inclusions are almost stagnant. Note that mean saltwater flux in the lower part of the saline wedge is landwards and upwards, but water flux at the low salinity inclusions is hindered by the low K and high density along their natural path. In short, seawater intrusion in heterogeneous media appears to display a long memory because of the near stagnation that is produced upstream (locally) of low K regions.

We show a detailed evolution of concentration maps in Figure 4.3 to gain further insight into the role of fluctuations and heterogeneity into the formation of low salinity inclusions. The figure displays four cycles (one per row), whereas columns represent the concentration maps at a given stage in the fluctuation. To facilitate interpretation, we have plotted arrows of the water flux (white for fresh water, purple for saltwater and fuchsia for mixing zone fluxes), as derived from a qualitative analysis of the pictures. The arrows in Figure 4.3 describe the assumed evolution between the stage where the arrows are plotted and the previous one. This requires thinking in terms of mass balance. For example, fuchsia fluxes are not easy to visualize as the images look pretty static. The task is somewhat facilitated by looking at the images like a movie or through a more detailed sequence of images for a cycle, which is shown in the appendix.

As expected, the fluxes are somewhat complex and radically different from what occurs in homogeneous media (see, e.g., Goswami and Clement (2007); Abarca and Prabhakar Clement (2009)), where (1) overall circulation in the seawater wedge is a counterclockwise (when sea is to the left), and (2) seawater enters horizontally into the medium and turns upwards sharply when reaching the mixing zone, which tends to be quite narrow. In our case, the mixing zone becomes wide (but far wider than for homogeneous media) only in the advancing portion of the cycle, when the upwards turn (fuchsia arrows) can be hinted. Seawater penetration is initially quite horizontal and non-uniform. While non-uniformity might be expected due to heterogeneity, the seawater advance is not dramatically longer along the high K regions. Instead, the advance appears to be somewhat hindered by the less saline inclusions left behind. Other than that, the wedge appears to accommodate itself (i.e., be limited by fresh water circulation). Towards the end of the cycle, intruding seawater tends to bend downwards, which is consistent with its high density, but contrary to homogeneous media.

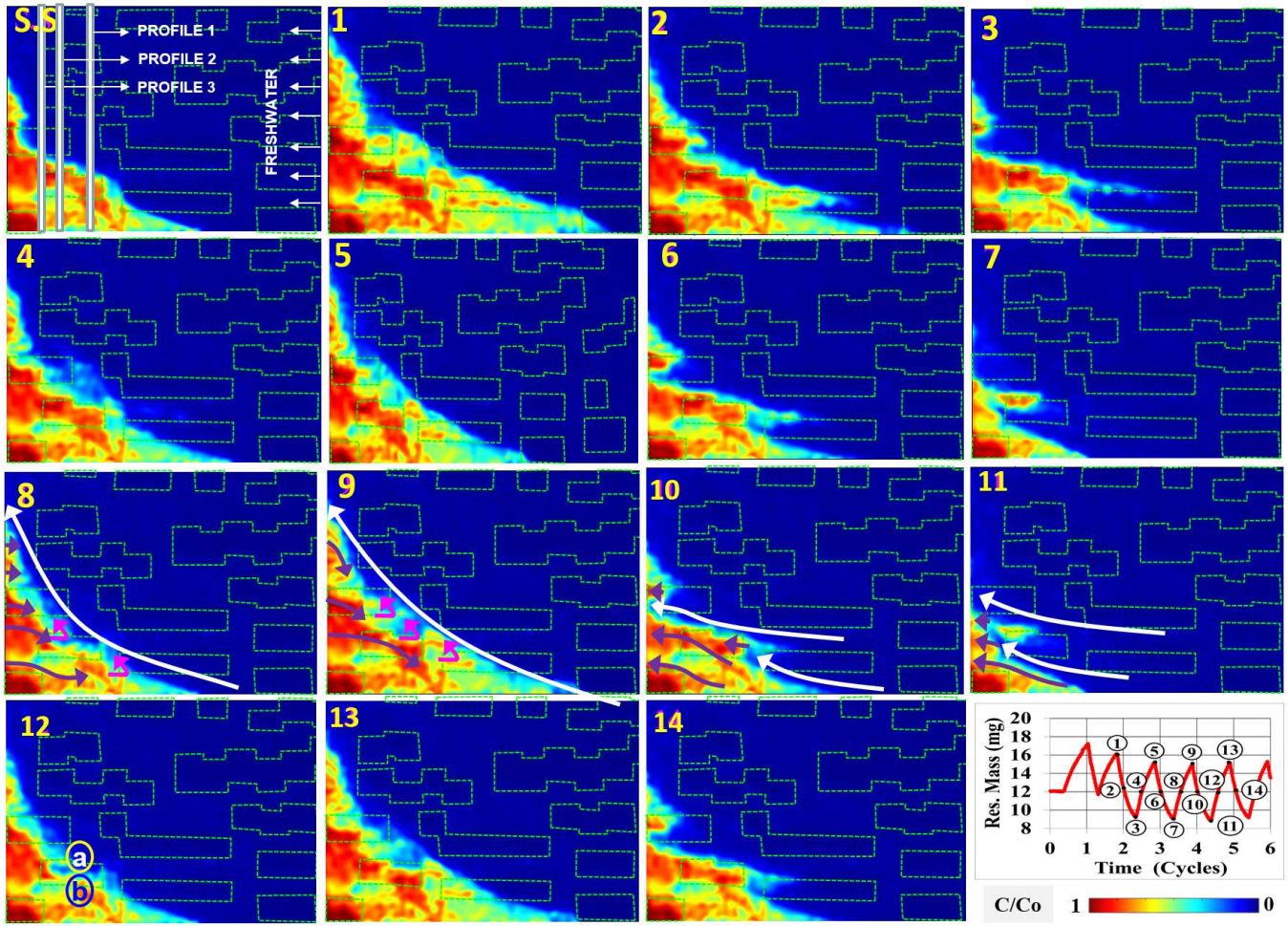

Figure 4.3: Evolution of seawater wedge in different times. Graphics present a different points in the evolution cycle. For each point we present the seawater wedge position

The appearance of the wedge changes dramatically during the receding portion of the cycle. Obviously, the wedge size decreases because it is pushed seawards by the build-up in freshwater pressure caused by the increase in freshwater discharge rate. What is more surprising, given the moderate heterogeneity of the medium, is that freshwater discharges through the middle of the wedge. Freshwater discharge trajectories do coincide with the high K connection to the sea. In fact, discharging freshwater floats over saline water, so that these trajectories occur in the upper portions of the coarse sand, just below fine sand blocks. This mechanism explains the apparently stagnant freshwater inclusions observed in our initial state. They are not really stagnant. They are renewed with freshwater during the wet season. This mechanism (fresh water flowing across the wedge) also explains why the ẗraditionalm̈ixing zone between the wedge and freshwater becomes highly compressed during the high flow (receding wedge) portions of the fluctuation cycles. Under steady flow conditions, the mixing zone is fed by seawater flowing horizontally from the sea and returns back to the sea along the interface between the wedge and the freshwater. However, this interface is disrupted by the discharging fresh water trajectories. As a result, the traditional mixing mechanism is discontinued during high flow periods. That is, mixing does not occur along the traditional interface between wedge and freshwater, but within the whole wedge. Another consequence of this stirring mechanism is that it helps in explaining the broad salinity profiles observed in the field, much broader than the narrow mixing zone derived from (quasi-)steady laboratory experiments and numerical models. Under (quasi) steady conditions, the mixing zone is controlled by local scale transverse dispersion, even in heterogeneous media (Held et al.). The time evolution of the salinity profiles in our experiments at three ideal locations is displayed in Figure 4.4. They are broad, highly fluctuating and non-monotonic. Note that mixing in the well would prevent recording non-monotonic profiles of this kind and tends to sharpen the salinity profile (Carrera et al., 2010). Therefore, the type of profiles of Figure 4.4 can only be detected sing induction measurements in closed well. Another consequence of the stirring mechanism is that the temporal average behavior does not represent the behavior observed at a given time (Figure 4.2). This questions the use of the ensemble average in stochastic theories. Stochastic research is often based on using the ensemble average as a practical form to resolve the complex problems. However, as we can see in Figure 4.2 (b), the temporal (ensemble) average behavior differs in shape, mass center, and, especially, thickness of mixing zone to those of any specific time (see, e.g., those of the initial, and maximum and minimum intrusion in Figure 4.2. In this case, the use of ensemble average for example in mixing estimation or mass transfer problems can lead to wrong results. The problem is similar to that of macrodispersion in traditional stochastic hydrology, which is much larger than effective dispersion due to fluctuations in the center of mass (Kitanidis, 1988; Dentz et al., 2000). However, non-linearity induced by density dependence makes things worse. It is worth pointing that some of the high salinity zones (e.g., those labeled a and b in Figure 4.3) appearing during the intruding portion of the cycle seem to be disconnected from the advancing high salinity fronts. The fact that these zones are repeated at every cycle implies that they are not visualization artifacts (every image was processed independently), but result from the structure of the medium. In fact, we conjecture that they may represent thin channels within the medium that only hit the walls at isolated points, similar to the ones displayed in Chapter 3. Like there, we conclude that the homogeneous advance that one might anticipate using continuum media understanding is insufficient. Even relatively homogeneous and uniform sands contain pore scale channels that favor the development of thin fingers ahead of advancing fronts. Obviously, these could only be visualized by means of refraction index matching porous media (Stohr et al., 2003; Ovdat and Berkowitz, 2006; Heyman et al., 2018), which has not been tried yet in SWI settings. The point, however is that this observation implies that dispersion is a pore scale process.

where the mixing zone thickness is different in all cases and has several changes if the wedge goes to the sea or intrude to the aquifer (Figure 4.3).

- Heterogeneity helps explaining sality profiles observed in the field, but rarely modelled
- Results show that the temporal average behavior does not represent the behavior observed at a given time. This questions the use of the ensemble average in stochastic theories.
- Mixing and spreading. We explain the increase in mixing by showing that the area between 10 and 25% increases.
- Mixing measure. We argue that this is not a good measure in this case. Transient with large fluctuations can change dispersion and the mixing.

Figure 4.2 (a) shows that it was not possible to have a S.S condition of seawater wedge. Previously, to start the fluctuation we injected saltwater for 4 hours. Photography showed that all zones are full with tracer but after to make the image process the result is no good.

4.3 shows seawater wedge evolution from different positions of evolution cycle starting with the SS conditions. We can see complex behavior when Freshwater comes out in the middle of the wedge (3, 4, 5, 6) where the depth of the mixing zone is several times higher.

4.4 Conclusions

We have performed laboratory experiments to assess the effect of coupling density variability, heterogeneity and time fluctuations, under conditions resembling those of seawater intrusion at a coastal aquifer. The description of the seawater intrusion that emerges from our experiments is very different from the traditional one. Seawater penetrates during dry periods quite horizontally, but tends to sink into the invaded freshwater because of the contrast in density (clockwise, when the sea is to the left). This causes active mixing within the wedge. Mixing also occurs at the ẗraditional interfaceät the boundary of the wedge, but not only by transverse dispersion. Longitudinal dispersion is also relevant, at least at the early stages. Pore scale dispersion is relevant during this stage. It would be hard to describe this process with Darcy-like continuum models. The seawater wedge is pushed seawards during wet periods, when transverse dispersion along the wedge boundary is hindered by freshwater flowing across the wedge along high K paths. As a result mixing is active within the wedge also during these periods. In short, coupling density dependence, (moderate) heterogeneity and (moderate) freshwater discharge fluctuations act like a stirring mechanism. A number of secondary observations result from this mechanism:

1) Coupling the three effects explains the salinity profiles observed in the field, but rarely modeled.
2) In fact, low permeability lenses in the salt-water intrusion wedge can create freshwater pools inside (and paths across) the sea water wedge.
3) SWI displays a long memory. True steady-state may take a long time. Even quasi-steady behavior also takes long and it depends on the initial conditions.
4) Time averaging leads to a SWI picture quite different from the behavior observed at any given time, which questions the use of the ensemble average in stochastic theories.

These observations imply that SWI may take place quite differently from the way it has been traditionally described. It is clear that further research is needed to confirm (or falsify) our conclusions and to start defining operating practical paradigms.

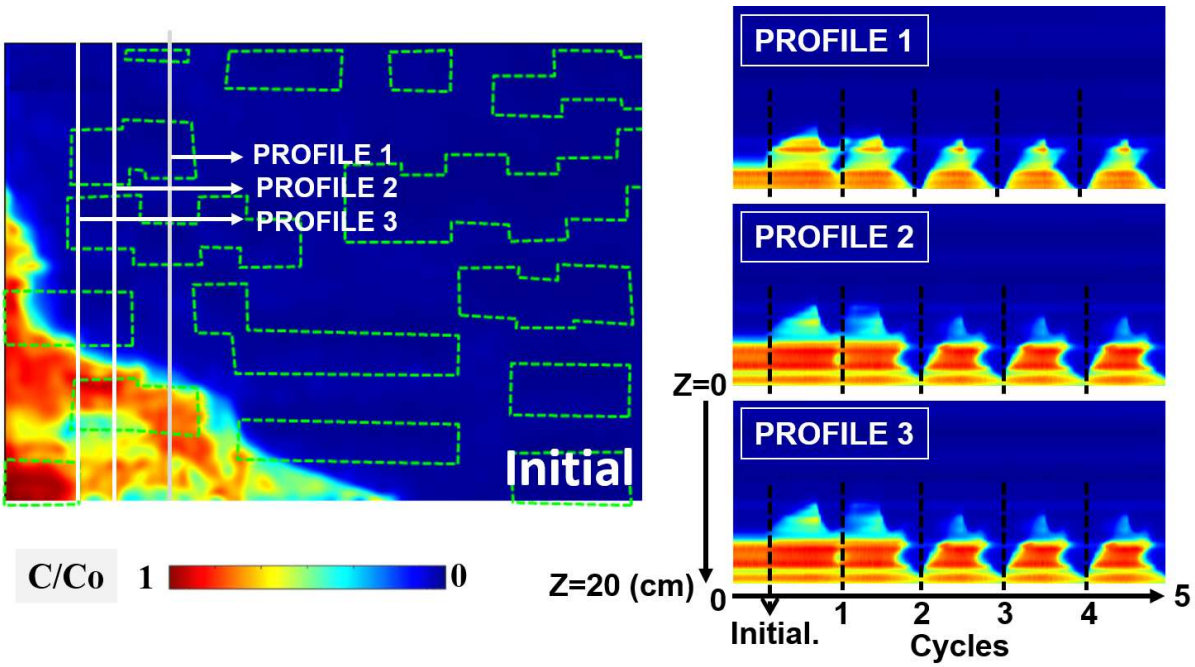

Figure 4.4: Profile concentration Evolution of seawater wedge in different times. This profile was stored in a Matrix (N,M). N is pixel (z) number, and M is time steps

Chapter 5

Conclusions

This thesis was motivated by the need to understand mixing processes under temporally fluctuating conditions, which we conjectured could accelerate mixing. Mixing is important because the rate of fast reactions is controlled by the rate at which reactants mix. Time fluctuations are ubiquitous in aquifers because groundwater flow boundary conditions and forcing terms fluctuate at all imaginable time scales. Therefore, understanding how mixing occurs through heterogeneous media under fluctuating conditions is a prerequisite for realistic modeling of the fate of pollutants in aquifers. We have performed laboratory experiments to gain understanding on mixing through tracer visualization. The first challenge was to overcome the difficulties associated to the noisy images produced by conventional image processing techniques. These images yield reliable, albeit noisy, concentration maps, but cannot be used to quantify mixing because it depends on concentration gradients squared, which are very sensitive to noise. In to overcome these problems, we developed a locally adapted kernel regression technique specifically designed to optimally smooth mixing. We applied this method to visualize the local mixing processes that occur during the injection and flushing of tracer in a heterogeneous porous medium. We found that our methodology was far superior to traditional image processing techniques in depicting local mixing processes. The experiment itself demonstrated that transverse gradients can be dominant at interfaces with high permeability contrasts within aquifers as well as in areas of relatively low velocity. As a result, regions of greatest reactions should not be expected only at the mixing front advancing in the direction of flow, but also along interfaces between zones of differing permeability. We have performed tracer experiments to evaluate the effect of flow fluctuations on solute transport behavior in a heterogeneous aquifer system. We compared concentration maps, visualized with the above methodology, and breakthrough curves obtained under steady-state flow to those obtained under fluctuating flow conditions. Experimental results indicate that the mean solute plume obtained with flow fluctuations is radically different from that obtained with steady-state flow conditions. Flow fluctuations tend to smooth solute plume fringes. Fluctuations appear to increase the accessibility of the solute tracer to the fine sand material, causing the entrapment of a large part of the solute tracer in low permeability inclusions. These processes do not affect the late-time behavior of the depth-average breakthrough curves measured at the tank outlet, which display the same slope as the steady-state ones, because the aquifer stratification was not severely modified. What fluctuations cause is a delay in the early time breakthrough. Combing this information with the changes observed in model parameters leads to the following main conclusions: (1) Flow fluctuations can enhance transverse mixing and mobile porosity; (2) the apparent longitudinal macrodispersion coefficient is increased due to flow fluctuations; (3) these effects appear to be controlled by the Kubo number (the effect of fluctuations is maximum when the Kubo number is close to one). Our third and final challenge was to assess the impact of seasonal recharge fluctuations on seawater intrusion in coastal aquifers. As above, this implies coupling heterogeneity and time fluctuations. But now, we also had to account for density dependent flow. To this end, we also performed laboratory experiments and visualized them with the methodology derived in this thesis. SWI has been traditionally viewed as consisting of a seawater wedge that rotates counter-clockwise (when sea is to the left) with fresh water flowing

above and mixing only at the interface by transverse dispersion. Our experiments suggest that (1) fresh water may flow through the wedge (during wet periods), (2) contains both clockwise and counter-clockwise circulation cells, (3) mixing occurs both at the interface and within the wedge, both by transverse and longitudinal dispersion, (4) fluctuation explain the salinity profiles observed in the field, but rarely modeled, (5) low permeability lenses in the wedge can create low salinity pools inside (and paths across) the sea water wedge, (6) SWI displays a long memory, and (7) time averaging leads to a SWI picture quite different from the behavior observed at any given time, which questions the use of the ensemble average in stochastic theories. These observations imply that SWI may take place quite differently from the way it has been traditionally described. It is clear that further research is needed to confirm (or falsify) our conclusions and to start defining operating practical paradigms. An observation from both sets of experiments is that pore scale dispersion is relevant. Pore scale channels precede advancing fronts. While they disappeared by fluctuations in the experiments of Chapter 3, which helps explaining why early arrival is delayed by fluctuations, they were essential to understand mixing in the experiments of Chapter 4. Therefore, we conclude that they are important. Yet, it would be hard to describe this process with Darcy-like continuum models.

Bibliography

Abarca, E., Carrera, J., Sánchez-Vila, X., Dentz, M., 2007. Anisotropic dispersive Henry problem. Advances in Water Resources 30, 913–926.

Abarca, E., Prabhakar Clement, T., 2009. A novel approach for characterizing the mixing zone of a saltwater wedge. Geophysical Research Letters 36, 1–5.

Andersen, M., 2001. Geochemical processes at a seawater-freshwater interface. Ph.D. thesis. Environment & Resources DTU. Technical University of Denmark.

Andersen, M.S., Nyvang, V., Jakobsen, R., Postma, D., 2005. Geochemical processes and solute transport at the seawater-freshwater interface of a sandy aquifer. Geochimica et Cosmochimica Acta 69, 3979 – 3994.

Ataie-Ashtiani, B., Ketabchi, H., 2010. Elitist Continuous Ant Colony Optimization Algorithm for Optimal Management of Coastal Aquifers. Water Resources Management 25, 165–190.

Aucour, A.M., Taoa, F.X., Moreira-Turcqb, P., Seylerc, P., Sheppardd, S., Benedetti, M., 2003. The amazon river: behaviour of metals (fe, al, mn) and dissolved organic matter in the initial mixing at the rio negro/solimes confluence. Chemical Geology 197, 271–285.

Ayora, C., Taberner, C., Saaltink, M., Carrera, J., 1998. The genesis of dedolomites: a discusion based on reactive transport modeling. Journal of Hydrology 209, 346–365.

Bear, J., 1972. Dynamics of Fluids In Porous Media. 1, American Elsevier Publishing Company.

Bear, J., 1988. Dynamics of Fluids in Porous Media. Dover.

Becker, M.W., Shapiro, A.M., 2000. Tracer transport in fractured crystalline rock: Evidence of nondiffusive breakthrough tailing. Water Resources Research 36, 1677.

Berkowitz, B., Cortis, A., Dentz, M., Scher, H., 2006. Modeling non-fickian transport in geological formations as a continuous time random walk. Rev. Geophys. .

Bolster, D., Valdes-Parada, F., Le Borgne, T., Dentz, M., Carrera, J., 2010. Mixing in confined stratified aquifers. J. Contam. Hydrol. 120-121, 10.1016/j.jconhyd.2010.02.00.

Burnett, W.C., Aggarwal, P.K., Aureli, A., Bokuniewicz, H., Cable, J.E., Charette, M.A., Kontar, E., Krupa, S., Kulkarni, K.M., Loveless, A., Moore, W.S., Oberdorfer, J.A., Oliveira, J., Ozyurt, N., Povinec, P., Privitera, A.M., Rajar, R., Ramessur, R.T., Scholten, J., Stieglitz, T., Taniguchi, M., Turner, J.V., 2006. Quantifying submarine groundwater discharge in the coastal zone via multiple methods. Science of the Total Environment 367, 498–543.

Carrera, J., Hidalgo, J., Slooten, L.J., Vázquez-Suné, E., 2010. Computational and conceptual issues in the calibration of seawater intrusion models. Hydrogeology journal 18, 131–145.

Carrera, J., Sánchez-Vila, X., I, B., Medina, A., Galarza, G., Guimera, J., 1998. On matrix diffusion: formulations, solutions methods and qualitative effects. Hydrogeology Journal 6, 178–190.

Castro-Alcalá, E., Fernaàndez-Garcia, D., Carrera, J., Bolster, D., 2012. Visualization of mixing processes in a heterogeneous sand box aquifer. Environmental Science and Technology 46, 3228–3235.

Cheng, a.H.D., Halhal, D., Naji, A., Ouazar, D., 2000. Pumping optimization in saltwater-intruded coastal aquifers. Water Resources Research 36, 2155–2165.

Cirpka, O., Frind, E.Oand Helming, R., 1999. Numerical simulation of biodegradation controlled by transverse mixing. Journal of Contaminant Hydrology 40, 159–182.

Cirpka, O.A., Attinger, S., 2003. Effective dispersion in heterogeneous media under random transient flow conditions. Water Resources Research 39, 1–15.

Cooper, H.H., 1959. A hypothesis concerning the dynamic balance of fresh water and salt water in a coastal aquifer. Journal of Geophysical Research 64, 461–467.

Corbella, M., Ayora, E., Cardellach, E., 2004. Hydrothermal mixing, carbonate dissolution and sulfide precipitation in mississippi valley-type deposits. MINERALIUM DEPOSITA 39 (3), 344–357.

Dagan, G., 1989. Flow and Transport in Porous Formations. Springer-Verlag Berlin Heidelberg.

Dagan, G., Bellin, A., Rubin, Y., 1996. Lagrangian analyisis of transport in heterogeneous fomrations under transient flow conditions. Water Resources Research 32, 891–899.

De Dreuzy, J.R., Carrera, J., Dentz, M., Le Borgne, T., 2012a. Asymptotic dispersion for two-dimensional highly heterogeneous permeability fields under temporally fluctuating flow. Water Resources Research 48. `W01532`.

De Dreuzy, J.R., Carrera, J., Dentz, M., Le Borgne, T., 2012b. Time evolution of mixing in heterogeneous porous media. Water Resources Research 48, 1–11.

De Dreuzy, J.R., Carrera, J., Dentz, M., Le Borgne, T., 2012c. Time evolution of mixing in heterogeneous porous media. Water Resources Research 48.

De Simoni, M., Carrera, J., Sanchez-Vila, X., Guadagnini, A., 2005. A procedure for the solution of multicomponent reactive transport problems. Water Resour. Res. 41, W11410. doi:10.1029/2005WR004056.

Dell'Oca, A., Porta, G.M., Guadagnini, A., Riva, M., 2018. Space-time mesh adaptation for solute transport in randomly heterogeneous porous media. Journal of Contaminant Hydrology 212, 28 – 40.

Dentz, M., Carrera, J., 2003. Effective dispersion in temporally fluctuating flow through a heterogeneous medium. Phys. Rev. E 68, 036310.

Dentz, M., Carrera, J., 2005. Effective solute transport in temporally fluctuating flow through heterogeneous media. Water Resources Research 41.

Dentz, M., Kinzelbach, H., Attinger, S., Kinzelbach, W., 2000. Transport behavior of a passive solute in continuuous time random walks and multirate mass transfer. Water Resources Research 39.

Domenico, P., 1990. Physical and chemical hydrogeology.

Donado, L.D.M., Sanchez-Vila, X., Dentz, M., Carrera, J., Bolster, D., 2009. Multicomponent reactive transport in milticontinuum media. Water Resour. Res. 45.

Du Commun, J., 1828. on the causes of fresh water spring, fountains. Am. J. Sci. 14, 174–176.

E., S.W., F., K.L., . Simulation of calcite dissolution and porosity changes in saltwater mixing zones in coastal aquifers. Water Resources Research 25, 655–667.

Emch, P.G., Yeh, W.W.G., 1998. Management model for conjunctive use of coastal surface water and ground water. Journal of Water Resources Planning & Management 124, 129.

Fernaàndez-Garcia, D., Sanchez-Vila, X., 2015. Mathematical equivalence between time-dependent single-rate and multirate mass transfer models. Water Resources Research 51, 3166–3180.

Fernàndez-Garcia, D., Llerar-Meza, G., Gómez-Hernández, J.J., 2009. Upscaling transport with mass models: Mean behavior and propagation of uncertainty. Water Resources Research 45.

Fernàndez-Garcia, D., Sanchez-Vila, X., 2011. Optimal reconstruction of concentrations, gradients and reaction rates from particle distributions. J. Contam. Hydrol. 120–121, 99–114.

Fernàndez-Garcia, D., Sanchez-Vila, X., Guadagnini, A., 2008. Reaction rates and effective parameters in stratified aquifers. Adv. Water Res. 31, 1364–1376.

Fetter, C., 1993. Contaminant hydrogeology.

Gamez, D., Simo, J., Lobo, F., Barnolas, A., Carrera, J., Vazquez-Sune, E., 2009. Onshore offshore correlation of the llobregat deltaic system, spain: Development of deltaic geometries under different relative sea level and growth fault influences. Sedimentary Geology 217, 65 – 84.

Garing, C., Luquot, L., Pezard, P., Gouze, P., 2013. Geochemical investigations of saltwater intrusion into the coastal carbonate aquifer of mallorca, spain. Applied Geochemistry 39, 1 – 10.

Gelhar, L., 1993. Stochastic Subsurface Hydrology.

Goode, D.J., Konikow, L.F., 1990. Apparent dispersion in transient groundwater flow. Water Resources Research 26, 2339–2351.

Goswami, R.R., Clement, T.P., 2007. Laboratory-scale investigation of saltwater intrusion dynamics. Water Resources Research 43, 1–11.

Gramling, C.M., Harvey, C.F., Meigs, L.C., 2002. Reactive transport in porous media: A comparison of model prediction with laboratory visualization. Environ. Sci. Technol. 36 (11), 2508–2514.

Haggerty, R., Gorelick, S.M., 1995. Multiple-rate mass transfer for modeling diffusion and surface reactions in media with pore-scale heterogeneity. Water Resources Research 31, 2383–2400.

Haggerty, R., McKenna, S.A., Meigs, L.C., 1998. On the late-time behavior of tracer test breakthrough curves. Water Resources Research 62, 62–74.

Haggerty, R., Reeves, P., 2002. STAMMT-L Version 1.0 Users Manual. Sandia Natl. Lab.

Hanshaw, B., Back, W., 1979. Major geochemical processes in the evolution of carbonate-aquifer systems. Journal of Hydrology 43(20), 287–312.

Hardle (Ed.), 1991. Smoothing Techniques, with Implementation in S. Springer Verlag.

Held, R., Attinger, S., Kinzelbach, W., . Homogenization and effective parameters for the henry problem in heterogeneous formations. Water Resources Research 41.

Henri, C.V., Fernàndez-Garcia, D., 2014. Toward efficiency in heterogeneous multispecies reactive transport modeling: A Particle-tracking solution for firts-order network reactions. Water Resources Research 50, 7206–7230.

Heyman, J., Turuban, R., Méheust, Y., Le Borgne, T., 2018. Transverse mixing in 3d porous flows: experimental results & stochastic inference, in: Computational Methods in Water Resources XXII, pp. 24–28.

Jose, S.C., Cirpka, O.A., 2004. Measurement of mixing-controlled reactive transport in homogeneous porous media and its prediction from conservative tracer test data. Environ. Sci. Technol. 38(7), 2089–2096.

Jose, S.C., Rahman, M.A., Cirpka, O.A., 2004. Large-scale sandbox experiment on longitudinal effective dispersion in heterogeneous porous media. Water Resources Research 40, 1–13.

Kapoor, V., Gelhar, L., 1994. Transport in threedimensionally heterogeneous aquifers: 1. dynamics of concentration fluctuations. Water Resour. Res. 30(6), 1775–1788.

Kim, K.Y., Chon, C.M., Park, K.H., 2007. A simple method for locating the fresh water-salt water interface using pressure data. Ground water 45, 723–8.

Kinzelbach, W., Ackerer, P., 1986. Modelisation de la propagation d'un contaminant dans un champ d'ecoulement transitoire. Hydrogeologie 2 2, 197–205.

Kitanidis, P.K., 1988. Prediction by the method of moments of transport in a heterogeneous formation. Journal of Hydrology 102, 453 – 473. Hydrologic Research: The U.S. mdash; Japan Experience.

Kitanidis, P.K., 1994. The concept of the dilution index. Water Resour. Res. 30(7), 2011–2026.

Knutson, C., Werth, C., Valocchi, A., 2005. Pore scale simulations of biomass growth along the transverse mixing zone of a model 2d porous medium. Water Resour. Res. 41, W07007.

Konz, M., Ackerer, P., Meier, E., Huggenberger, P., Zechner, E., Gechter, D., 2008. On the measurement of solute concentrations in 2-d flow tank experiments. Hydrol. Earth Syst. Sci. 12, 727–738.

Kreft, A., Zuber, A., 1978. On the fisical meaning of the dispersion equation and its solutions for different initial and boundary conditions. Chem. Eng. Sci. 33, 1471–1480.

Kuan, W.K., Jin, G., Xin, P., Robinson, C., Gibbes, B., Li, L., 2012. Tidal influence on seawater intrusion in unconfined coastal aquifers. Water Resources Research 48, 1–11.

Lachassagne, P., Wyns, R., Dewandel, B., 2011. The fracture permeability of hard rock aquifers is due neither to tectonics, nor to unloading, but to weathering processes. TERRA NOVA 23 (3), 145–161.

Langevin, C.D., 2003. Simulation of Submarine Ground Water Discharge to a Marine Estuary: Biscayne Bay, Florida. Ground Water 41, 758–771.

Le Borgne, T., Dentz, M., Bolster, D., Carrera, J., Dreuzy, J.R., Davy, P., 2010. Non-fickian mixing: temporal evolution of the scalar dissipation rate in porous media. Advances in Water Resources 33(12), 1468–1475.

Levy, M., Berkowitz, B., 2003. Measurement and analysis of non-Fickian dispersion in heterogeneous porous media. Journal of Contaminant Hydrology 64, 203–226.

Li, L., Barry, D.A., Stagnitti, F., Parlange, J.Y., 1999. Submarine groundwater discharge and associated chemical input to a coastal sea. Water Resources Research 35, 3253–3259.

Lindstrom, F.T., Haque, R., Freed, V.H., Boersma, L., 1967. The movement of some herbicides in soils. linear diffusion and convection of chemicals in soils. Environ. Sci. Technol. 1, 561–565.

Lu, C., Luo, J., 2010. Dynamics of freshwater-seawater mixing zone development in dual-domain formations. Water Resources Research 46, 1–6.

Luo, J., Dentz, M., Carrera, J., Kitanidis, P., 2008. Transport controlled effective reaction parameters in heterogeneous media. Water Resour. Res. 44 (2).

MacCready, P., Geyer, W.R., 2010. Advances in Estuarine Physics. Annual Review of Marine Science 2, 35–58.

Mantoglou, A., Papantoniou, M., Giannoulopoulos, P., 2004. Management of coastal aquifers based on nonlinear optimization and evolutionary algorithms. Journal of Hydrology 297, 209–228.

María, P., A., P.V.E., T., S.C., 2015. Effects of tidal fluctuations and spatial heterogeneity on mixing and spreading in spatially heterogeneous coastal aquifers. Water Resources Research 51, 1570–1585.

Mckenna, S.A., Meigs, L.C., Haggerty, R., 2001. Tracer tests in a fractured dolomite: 3. double-porosity, multiple-rate mass transfer processes in convergent flow tracer tests. Water Resources Research 37, 1143–1154.

McNeil, J., Oldenborger, G., Schincariol, R., 2006. Quantitative imaging of contaminant distributions in heterogeneous porous media laboratory experiments. J. Contam. Hydrol. 84, 39–54.

Moore, C.H., 1973. Intertidal Carbonate Cementation Grand Cayman, West Indies. Journal of sedimentary petrology 43, 591–602.

Moore, W.S., 2010. The Effect of Submarine Groundwater Discharge on the Ocean. Annual Review of Marine Science 2, 59–88.

Naji, A., Cheng, A.H., Ouazar, D., 1999. BEM solution of stochastic seawater intrusion problems. Engineering analysis with boundary elements 23, 529–537.

Nnambi, I., Werth, C., Sanford, R., Valocchi, A., 2003. Pore-scale analysis of anaerobic halorespiring bacterial growth along the transverse mixing zone of an etched silicon pore network. Environ. Sci. Technol. 37, 5617–5624.

Ovdat, H., Berkowitz, B., 2006. Pore-scale study of drainage displacement under combined capillary and gravity effects in index-matched porous media. Water Resources Research 42.

Park, C.H., Aral, M.M., 2004. Multi-objective optimization of pumping rates and well placement in coastal aquifers. Journal of Hydrology 290, 80–99.

Park, N., Cui, L., Shi, L., 2009. Analytical design curves to maximize pumping or minimize injection in coastal aquifers. Ground Water 47, 797–805.

Parker, J.C., Genuchten, M.T., 1984. Flux-averaged and volume-averaged concentrations in continuum approaches to solute transport. Water Resources Research 20, 866–872.

Paster, A., Dagan, G., 2008. Mixing at the interface between two fluids in aquifer well upconing steady flow. Water Resources Research 44, 1–11.

Pedretti, D., Fernàndez-Garcia, D., Bolster, D., Sanchez-Vila, X., 2013. On the formation of breakthrough curves tailing during convergent flow tracer tests in three-dimensional heterogeneous aquifers. Water Resources Research 49, 4157–4173.

Pool, M., Carrera, J., 2011. A correction factor to account for mixing in ghyben-herzberg and critical pumping rate approximations of seawater intrusion in coastal aquifers. Water Resources Research 47.

Pool, M., Post, V.E., Simmons, C.T., 2014. aquifers : Homogeneous case. Water Resources Research , 6910–6926.

Pope, S.B., 2000. Stochastic lagrangian models of velocity in homogeneous turbulent shear flow. Physics of Fluids 14, 1696–1702.

Price, R.M., Top, Z., Happell, J.D., Swart, P.K., 2003. Use of tritium and helium to define groundwater flow conditions in Everglades National Park. Water Resources Research 39, 1–12.

QAHMAN, K., LARABI, A., OUAZAR, D., NAJI, A., CHENG, A.H.D., 2009. Optimal Extraction of Groundwater in Gaza Coastal Aquifer. Journal of Water Resource and Protection 01, 249–259.

R., H., L., T.M., F., M.J., 1987. Method of Estimating the Travel Time of Noninteracting Solutes Through Compacted Soil Material. Soil Sci. Soc. Am. J 51, 48–53.

Raeisi, E., Mylroie, J., 1979. Hydrodynamic behavior of caves formed in the fresh-water lens of carbonate islands. Carbonates and Evaporites 10, DOI: 10.1007/BF03175405.

Rahman, A., S., J., W., N., Cirpka, O., 2005a. Experiments on vertical transverse mixing in a large-scale heterogeneous model aquifer. J. Contam. Hydrol. 80, 130–148.

Rahman, M.A., Jose, S.C., Nowak, W., Cirpka, O.A., 2005b. Experiments on vertical transverse mixing in a large-scale heterogeneous model aquifer. Journal of Contaminant Hydrology 80, 130–148.

Raje, D.S., Kapoor, V., 2000. Experimental study of bimolecular reaction kinetics in porous media. Environ. Sci. Technol. 34 (7), 1234– 1239.

Rehfeldt, K., Gelhar, L., 1992. Stochastic analysis of dispersion in unstaedy flow in heterogeneous aquifers. Water Resour. Res. 28, 2085–2099.

Reinelt, P., 2005. Seawater intrusion policy analysis with a numerical spatially heterogeneous dynamic optimization model. Water Resources Research 41, 1–12.

Rezaeia, M., Sanz, E., Raeisia, E., Ayora, C., Vásquez-Suné, E., Carrera, J., 2005. Reactive transport modeling of calcite dissolution in the fresh-salt water mixing zone. Journal 311, 282–298.

Riva, M., Guadagnini, A., Fernàndez-Garcia, D., Sanchez-Vila, X., Ptak, T., 2008. Relative importance of geostatistical and transport models in describing heavily tailed breakthrough curves at the Lauswiesen site. Journal of Contaminant Hydrology 101, 1–13.

Runnels, D., 1969. Diagenesis, chemical sediments, and the mixing of natural waters. Journal of Sedimentary Petrology 39, 1188–1201.

Sanchez-Vila, X., Guadagnini, A., Fernández-Garcia, D., 2009. Conditional probability density functions of concentrations for mixing-controlled reactive transport in heterogeneous aquifers. Mathematical Geosciences 41, 323–351, doi:10.1007/s11004–008–9204–2.

Schincariol, R., Herderick, E., Schwartz, F., 1993. On the application of image analysis to determine concentration distributions in laboratory experiments. J. Contam. Hydrol. 12, 197–215.

Simpson, M., Clement, T., 2003. Theoretical analysis of the worthiness of henry and elder problems as benchmarks of density-dependent groundwater flow models. Advances in Water Resources 26, 17 – 31.

Stohr, M., Roth, K., Jahne, B., 2003. Measurement of 3d pore-scale flow in index-matched porous media. Exp Fluids 35.

Sudicky, A., 1986. A natural gradient experiment on solute transport in a sand aquifer : Spatial variability of hydraulic conductivity and its role in the dispersion process. Water Resources Research 22, 2069–2082.

Swartz, C.H., Schwartz, F.W., 1998. An experimental study of mixing and instability development in variable-density systems. J. Contam. Hydrol. 34, 169–189.

Sykes, J.F., Pahwa, S.B., Lantz, R.B., Ward, D.S., 1982. Numerical simulation of flow and contaminant migration at an extensively monitored landfill. Water Resources Research 18, 1687–1704.

Takeda, H., Farsiu, S., Milanfar, P., 2007. kernel regression for image processing and reconstruction. IEEE Transactions on Acoustics, Speech and Signal Processing 16, 349–366.

Volker, R., 2002. Numerical modelling of contaminant transport in coastal aquifers. Mathematics and Computers in Simulation 59, 35–44.

Weeks, C.W., Sposito, G., 1998. Mixing and stretching efficiency in steady and unsteady groundwater flows. Water Resour. Res. 34, 3315–3322.

Werner, A.D., Ward, J.D., Morgan, L.K., Simmons, C.T., Robinson, N.I., Teubner, M.D., 2012. Vulnerability indicators of sea water intrusion. Ground Water 50, 48–58.

Willingham, T., Werth, C., Valocchi, A., 2008. Evaluation of the effects of porous media structure on mixing-controlled reactions using pore-scale modeling and micromodel experiments. Environ. Sci. Technol. 49 (2), 3185–3193.

Willis, R., Finney, B.A., 1988. Planning model for optimal control of saltwater intrusion. Journal of Water Resources Planning and Management 114, 163–178.

Willmann, M., Carrera, J., Sanchez-Vila, X., 2008. Transport upscaling in heterogeneous aquifers: What physical parameters control memory functions? Water Resour. Res. 46.

Willmann, M., Carrera, J., Sanchez-Vila, X., Silva, O., Dentz, M., 2010. Coupling of mass transfer and reactive transport for nonlinear reactions in heterogeneous media. Water Resour. Research 44.

Wood, B.D., Cherblanc, F., Quintard, M., Whitaker, S., 2003. Volume averaging for determining the effective dispersion tensor: Closure using periodic init cells an comparison with ensemble averaging. Water Resources Research 39.

Xue, Y., Wu, J., Liu, P., Wang, J., Jiang, Q., Shi, H., 1993. Sea-water intrusion in the coastal area of laizhou bay, china : 1.distribution of sea-water intrusion and its hydrochemical characteristics. Ground Water 31, 532– 537.

Zhang, C., Dehoff, K., Hess, N., Oostrom, M., Wietsma, T.Wand Valocchi, A.J., Fouke, B.W., Werth, C., 2010a. Pore-scale study of transverse mixing induced $caco_3$ precipitation and permeability reduction in a model subsurface sedimentary system. Environ. Sci. Technol. 44 (20), 7833–7838.

Zhang, C., Kang, Q., Wang, X., Zilles, J., Muller, R., J., C., Werth, C., 2010b. Effects of pore-scale heterogeneity and transverse mixing on bacterial growth in porous media. Environ. Sci. Technol. 44 (8), 3085–3092.

Zhang, D., Neuman, S.P., 1996. Io s s ' P (s ') ds '. Water Resources Research 32, 77–83.

Zhang, Q., Volker, R.E., Lockington, D.A., 2002. Experimental investigation of contaminant transport in coastal groundwater. Advances in Environmental Research 6, 229 – 237.